



UNIVERSITY OF AMSTERDAM

## MSc Physics

Advanced Matter and Energy Physics

Master Thesis

---

# Indirect to direct bandgap transition in methylammonium lead halide perovskite

Exploring the optoelectronic properties of novel solar cell material

---

*by*

**Benjamin Daiber**

**Stud.nr: 10890025**

*July 2016*

*60 ECTS*

*September 2015 - July 2016*

*1<sup>st</sup> Examiner:*

Prof. Albert POLMAN

*Supervisor:*

Dr. Bruno EHRLER

*2<sup>nd</sup> Examiner:*

Prof. Tom GREGORKIEWICZ



Benjamin Daiber: *Indirect to direct bandgap transition in methylammonium lead halide perovskite*, Exploring the optoelectronic properties of novel solar cell material, © July 2016

Nobody ever figures out what life is all about, and it doesn't matter.  
Explore the world. Nearly everything is really interesting if you go  
into it deeply enough.

— Richard P. Feynman



## ABSTRACT

---

Methylammonium lead iodide (MAPI) is thought to be a direct band gap semiconductor. The nature of this direct bandgap stands in contrast to the long charge carrier lifetimes of up to  $15\,\mu\text{s}$  that this material exhibits. I present experimental evidence for the presence of an indirect transition  $60\,\text{meV}$  below the direct transition. Charge carriers in (MAPI) decay *via* an indirect transition, requiring a phonon for the decay. The necessary phonon contribution renders the decay inefficient, thus slow.



*If I have seen further, it is by standing on the shoulders of giants.*

— Isaac Newton, 1676

## ACKNOWLEDGMENTS

---

I would like to thank:

Foremost TianYi Wang for a great collaboration, help and discussions. Bruno Ehrler for supervision, great ideas regarding the development of the project and the opportunity of conducting my research project in his lab. I hope for good things to come. Albert Polman for being first examiner. Tom Gregorkiewicz for being second examiner and the opportunity to do the AMEP lab project in his lab that got me interested in solar cells. Sander Mann for discussions about the charge carrier density and its influences. Sarah Brittman for help with the [TCSPC](#) setup and discussions. Moritz Futscher for the occasional MATHEMATICA help. Jumin Lee for help with the evaporator. Le Yang for the use of her solar cells. All other former and current members of the Hybrid Solar Cells group at AMOLF for a nice working atmosphere and interesting discussions at the lunch table. The AMOLF workshop for their mechanical prowess. Ricardo Struik for designing the sample holders. My office mates Annemarie Berkhout, Giada la Gala, and Remmert Muller for a nice work environment. Jennifer Lamphere for emotional support, existing in this world, and native speaker proof-reading services.





# CONTENTS

---

1	INTRODUCTION TO PEROVSKITES	1
1.1	Overview of possible explanations	4
1.1.1	Triplet excitons	4
1.1.2	Polarons	4
1.1.3	Microstructure	5
1.2	Indirect bandgap caused by rashba splitting	5
1.3	Experimental Methods	8
1.3.1	Sample preparation	8
1.3.2	Pressure induced band structure change	8
1.4	Structure of this work	10
2	PHOTOLUMINESCENCE SPECTRA UNDER PRESSURE	11
2.1	Methods	11
2.2	Results	11
2.3	Discussion	12
2.4	Competing explanations	15
3	TRANSIENT PHOTOLUMINESCENCE OF MAPI UNDER PRESSURE	17
3.1	General working techniques of TCSPC	17
3.2	Measurement procedure	18
3.3	Measurement data	19
3.4	Model to describe data	20
3.5	Fitting procedure	21
3.6	Extraction of decay path importance	24
3.6.1	Ratio of decay paths	26
3.7	Justification of assumptions in model	26
3.7.1	Auger term	27
3.7.2	Treatment of electrons and holes as charge carriers	28
3.7.3	Photodiode test	28
3.7.4	Initial charge carrier density influence	29
3.7.5	Global fit	31
3.8	Charge carrier density calculation	31
4	ABSORBANCE SPECTRA REANALYSIS	35
4.1	introduction to tauc rule	35
4.2	Phonon energy	36
4.3	Linearization of data with fit	36
4.4	Urbach tail	37
4.5	resulting absorbance plot	37
5	ELECTRICAL PROPERTIES OF MAPI UNDER PRESSURE	39

5.1	Setup	39
5.2	Measurement in the dark	40
5.2.1	Theory	40
5.2.2	Fit of Theory	42
5.2.3	Direct calculation using literature parameters	42
5.3	Measurement under illumination	43
6	CONCLUSION AND OUTLOOK	47
6.1	Conclusion	47
6.2	Outlook	47
	BIBLIOGRAPHY	49

## LIST OF FIGURES

Figure 1	absorption coefficients	2
Figure 2	Bandgap schematics	3
Figure 3	MAPI tilting	6
Figure 4	Schematics of MAPI bands	7
Figure 5	Pressure cell	9
Figure 6	PL spectra	12
Figure 7	PL Main to Side peak area	13
Figure 8	Schematics: Pressure-induced bandstructure change	13
Figure 9	PL Main to Side peak position	14
Figure 10	PL at high and low excitation power	14
Figure 11	TCSPC setup	18
Figure 12	IRF of TCSPC-setup	19
Figure 13	Raw Time Correlated Single Photon Counting (TCSPC)-data with fit	20
Figure 14	P-Values of fit	24
Figure 15	Residuals of $p < 0.05$	25
Figure 16	radiative and non-radiative rates	25
Figure 17	Fraction of radiative and nonradiative decay	27
Figure 18	Auger: Decays at different excitation energies	28
Figure 19	Variation of excitation power	29
Figure 20	Theoretic curves with constant $k_R$ and $k_{NR}$	30
Figure 21	Change of $k_R$ and $k_{NR}$ with excitation density	30
Figure 22	Global fit on high charge carrier density data	32
Figure 23	Beam profile	33
Figure 24	Tauc Plot of direct and indirect band edge	37
Figure 25	PDS Absorbance with indirect and direct fit	38
Figure 26	Resistance sketch	39
Figure 27	Resistance measurement protocol	40
Figure 28	Resistance data in dark	40
Figure 29	Resistance in the dark	42
Figure 30	IV-Curves under illumination	43
Figure 31	Resistance under illumination	44

## LIST OF TABLES

Table 1	Solution of two process model	21
---------	-------------------------------	----

ACRONYMS

---

MA	Methylammonium
FA	Formamidinium
MAPI	Methylammonium lead iodide
PL	Photoluminescence
TCSPC	Time Correlated Single Photon Counting
IRF	Instrument Response Function
FWHM	Full Width at Half Maximum
UV-Vis	Ultraviolet-Visible light absorbance
PDS	Photothermal Deflection Spectroscopy
IV	Current Voltage
LED	Light Emitting Diode

## INTRODUCTION TO PEROVSKITES

---

In the next two decades the primary energy consumption is expected to rise by 50% [1]. Growing energy needs warrant a solution that can generate electricity without generating CO<sub>2</sub>. Especially underdeveloped, non-OECD countries are likely to retract to coal, gas, and oil power plants to supply their energy needs, just as early 1900s Europe and United States have done. This could lead to dramatically increased CO<sub>2</sub> output that endangers humanity's survival on large parts of the globe. Poor countries cannot afford countermeasures to the changing climate and are therefore most affected by environmental changes. Since wave, hydrogeology, and wind power plants have already been largely installed in the most cost efficient places, the only practically unlimited and scalable source of CO<sub>2</sub> neutral and cheap energy remains to be photovoltaics [2]. Great advances have been achieved in making standard silicon solar cells cheaper. As time progresses, it becomes increasingly hard to improve on this highly engineered material.

*Why photovoltaics?*

In addition to silicon, several new materials are currently being investigated as cheap and efficient alternatives that could replace silicon in the mid to distant future. One of these emergent materials is the class of crystals called perovskites. Perovskites are defined by an ABX<sub>3</sub> crystal structure with a wide variability of possible elements on the respective A, B, and X sites. In perovskites used for solar cells the A site is either an organic (e.g. Methylammonium (MA) or Formamidinium (FA)) or inorganic (e.g. Cesium) cation; the B site is occupied by a metal cation (e.g. lead, copper, or tin); the X site is occupied by a halide anion (e.g. iodide or bromide). Methylammonium lead iodide (MAPI) is one material that is particularly interesting because it is the "prototypical" perovskite with the largest body of research conducted, the high solar cell efficiencies of 17% [3] and "clean" structure lacking a mixture of perovskite types. MAPI has a CH<sub>3</sub>NH<sub>3</sub><sup>+</sup> ion on the A site, a lead atom on the B site, and three iodine atoms on the X site, surrounding the lead (Fig. 3). This work studies the properties of MAPI exclusively.

*Why MAPI?*

The following chapter gives an overview of the mechanisms of charge carrier generation and decay in MAPI. The main task of a solar cell is to absorb energy in the form of light and to convert it into usable electrical energy. This can be very crudely split into two parts. Firstly, light absorption, resulting in charge carrier generation, and subsequently the extraction of those charge carri-

ers. Light is absorbed if the photon energy is higher than the intrinsic bandgap energy of the semiconductor. The absorption efficiency depends on the material, and more specifically on the nature of the bandgap, being either direct or indirect. A bandgap is considered to be direct if there is no additional lattice vibration (phonon) needed for the absorption process to happen. Direct bandgap semiconductors generally exhibit strong absorption. In contrast, an indirect bandgap has less efficient absorption, since the absorption process requires an additional phonon.

Consequently, the absorption coefficient of the direct bandgap semiconductor gallium arsenide is about one order of magnitude higher than that of the indirect semiconductor silicon. [MAPI](#) is known to be a direct bandgap semiconductor, and exhibits strong absorption (Fig. 1).

*How does MAPI  
absorb light?*

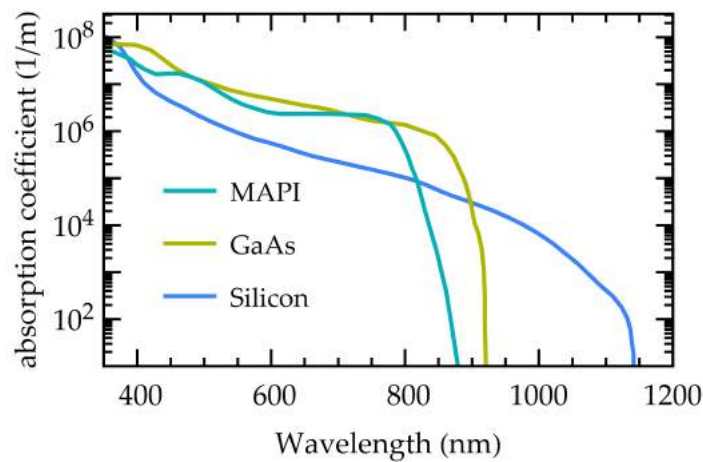


Figure 1: Absorption coefficient of crystalline silicon, gallium arsenide, and [MAPI](#) taken from [4, 5]. Silicon, being an indirect semiconductor has lower absorption than the direct semiconductors gallium arsenide and [MAPI](#)

After the photon is absorbed, a free electron and hole pair is created. So-called holes are particles with a positive elementary charge that arise when an electron is missing from the neutrally charged crystal lattice. Upon creation, the hole has the exact opposite momentum of the electron, due to momentum conservation. In many organic compounds the two charge carriers (electrons and holes) are still bound to each other and cannot move freely. This bound state is called exciton. In organic materials this is the only species that is populated after the absorption of a photon. In these systems the binding energy is high ( $\sim$  eV) which means that the thermal energy at room temperature ( $k_B T \sim 25$  meV) is not sufficient to overcome the binding energy. In [MAPI](#) perovskites different binding energies ranging from 10 meV to 60 meV have been reported [6]. Lately, the field has converged towards the view that the binding energy is low, leading to free charge

*Are there free  
charges?*

carriers being the dominating species [6]. In this study charge carriers are assumed to be free.

Following the generation of free charges, the carriers have to be extracted before they decay and the energy is lost to heat. Whether effective extraction can happen depends on the thickness of the active solar cell material. The thickness should be on the same order or smaller than the diffusion length.

$$L_d = \sqrt{D\tau} \quad (1)$$

With the diffusivity  $D$  and the lifetime of the charge carriers  $\tau$ . This shows that the efficiency of charge carrier extraction is directly related to charge carrier lifetime.

Charge carriers have two main decay channels at low charge carrier density; monomolecular<sup>1</sup> decay, which is thought to be trap mediated and dark, and bimolecular decay involving two charge carriers that recombine and emit a photon of bandgap energy.

Absorption and emission of photons are governed by the same transition matrix element. A material with a high absorption coefficient therefore usually has short lived charge carriers and *vice versa*. This can also be understood *via* the nature of the bandgaps. Indirect bandgap semiconductors require a phonon to emit a photon (which has no net momentum). The photon emission process (PL) is therefore less efficient in an indirect semiconductor in comparison to a direct semiconductor. Hence, there is a trade off between absorption efficiency and charge carrier extraction efficiency. The direct semiconductor gallium arsenide has a charge carrier lifetime in the  $\sim$  ns range, the indirect semiconductor silicon has a charge carrier lifetime in the  $\sim$  ms range [7].

*Why does the lifetime matter?*

*Is there a connection of bandgap to absorption and lifetime?*

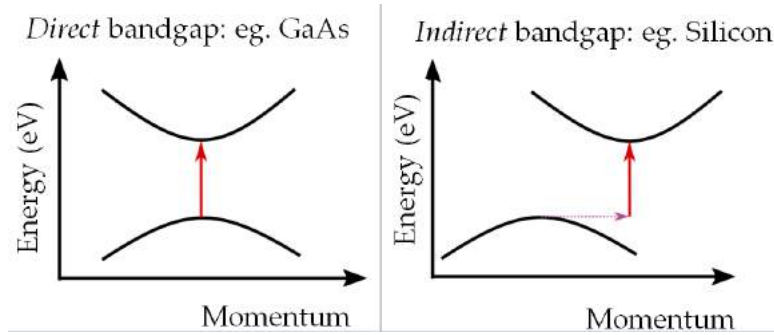


Figure 2: Bandgap schematics of a direct (left) and indirect (right) semiconductor. Arrows depict absorption processes.

Surprisingly, this fundamental principle seems not to apply in [MAPI](#) perovskites. [MAPI](#) is known to be a direct semiconductor with efficient absorption (Fig. 1), but it also has very long charge carrier lifetimes

*Why is MAPI so special?*

<sup>1</sup> decay involving only one charge carrier

in the range<sup>2</sup> of  $\sim \mu\text{s}$ , and thus efficient charge carrier collection. Both high absorption and good charge carrier collection enables the high solar cell efficiency in [MAPI](#). Unraveling the seemingly contradicting properties of direct bandgap and long carrier lifetime are the main topic of this work.

### 1.1 OVERVIEW OF POSSIBLE EXPLANATIONS

Many possible explanations have been developed in the literature to address this seemingly contradictory behavior, responsible for the high solar cell performance of [MAPI](#) perovskites. Three will be shortly investigated below.

#### 1.1.1 *Triplet excitons*

Fang et al. assign the long lived states in [MAPI](#) to triplet excitons [8]. It seems that the main motivation for doing so is the long charge carrier lifetime in the  $\mu\text{s}$  range. The exchange energy which determines the difference in energy between singlet to triplet state is measured to be 80 meV, which is large in comparison with the theoretically expected value of 2 meV, as the authors note themselves. Also, the reported increasing importance of the side peak with lower temperature does not fit into the triplet picture.

For triplet excitons to develop from singlet excitons, singlet excitons have to be the majority species. However, as mentioned before, free charge carriers are seen to be the majority charge carriers. The requirement of existing singlet excitons in [MAPI](#) seems therefore not to be met. If there would be sufficient singlet exciton states, the high intersystem crossing rate given by the heavy elements in [MAPI](#) would also result in a short lifetime of triplet states.

#### 1.1.2 *Polarons*

Zhu and Podzorov suggest that charge carriers are protected from electron-phonon scattering by forming large polarons [9]. The screening would lead to prolonged lifetimes. A polaron is a coherent motion of many lattice subunits, which allows for coherent transport of charge carriers. The [MA](#) ion in the middle of the cage is here vital for the formation of the polaron because it supplies the needed electrostatic potential. However, long charge carrier lifetimes are also reported in perovskites containing cesium on the A site. Cesium, being an atom, has no dipole moment and would therefore not supply an electric field, raising questions about the range of materials in which

<sup>2</sup> Depending on crystal quality, deposition methods, used precursor, and sample age.



polarons can explain long charge carrier lifetimes. This explanation might model some features of [MAPI](#), but direct proof of their existence has not yet been found.

### 1.1.3 Microstructure

Quilettes et al. notes that the lifetime and PL intensities vary greatly between grains of the same material [10]. Especially the boundaries of the grains exhibit different lifetimes, suggesting that the micro structure has an important impact on the macro scale behavior. Faster charge carrier decay is attributed to traps at the grain boundaries, which also explains the locally reduced Photoluminescence (PL) intensity.

## 1.2 INDIRECT BANDGAP CAUSED BY RASHBA SPLITTING

In this work I will show that the long charge carrier lifetimes in [MAPI](#), a direct bandgap semiconductor, result from a slightly indirect transition, appearing 60 meV below the direct transition (schematics seen in Fig. 4).

*Is the bandgap really direct?*

This indirect transition appears due to spin-orbit coupling, made possible by the presence of a heavy element, lead, and an electric field lifting the degeneracy in energy between the spin states. The band structure that describes the electron energy landscape has been calculated in many different ways; recently [11] have presented a quasi particle self consistent treatment of the problem and have found a spin orbit split of the conduction band in the wavevector space.

The conduction band is residing mainly on the lead atom in the middle of the lead-iodide sub-lattice cage. Lead is a very heavy atom with an atomic number of 82, meaning that the spin orbit coupling of its electrons is strong<sup>3</sup>. The valence band is mainly located around the iodide atoms, which have a lower mass and therefore lower spin orbit coupling. The existence of a net electric field, which can be caused by the [MA](#) ion and lead-iodide sub-lattice tilting, allows for a energy split of the normally degenerate spin up and down states in electron wavevector space. The so called Bychkov-Rashba Hamiltonian describes this system [13]:

$$\mathcal{H} = \frac{\mathbf{p}^2}{2m} - \underbrace{\alpha' \frac{\hbar}{4m^2c^2}}_{\alpha/\hbar} \boldsymbol{\sigma} \cdot (\mathbf{p} \times \nabla V) \quad (2)$$

where

<sup>3</sup> The spin orbit coupling scales with  $Z^2$  [12]

$\mathbf{p}$	electron momentum
$m$	electron mass
$\alpha'$	strength of the spin orbit coupling
$\sigma$	spin Pauli matrix
$\nabla V$	gradient of the potential

The potential  $\nabla V$  can arise in crystals lacking inversion symmetry [14]. There is an electrical field contribution from the tilting of the lead-iodide cage in at least one plane of the crystal, as well as an influence of the MA ion, which can also add to the total electrical field.

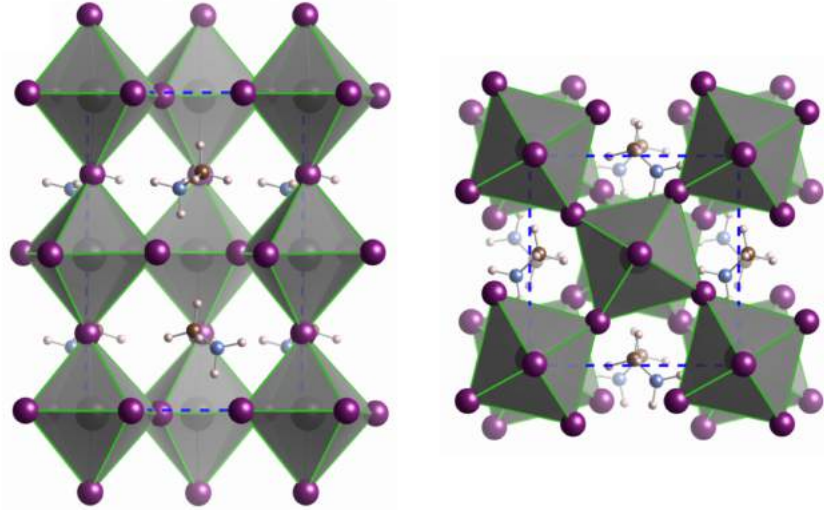


Figure 3: Tilting of the **MAPI** sub-lattices in the tetragonal phase, present at ambient conditions. *Left*: view from  $\langle 100 \rangle$  direction; *Right*: view from  $\langle 001 \rangle$  direction. Iodine atoms are depicted in violet and surround the lead atoms; the floating molecule is **MA**. The tilting is one source of an electrical potential acting on the led orbitals and lifting the energy degeneracy. Taken from [15] under CC 3.0 license

The first part of the Hamiltonian is the normal case without spin orbit coupling, leading to parabolic bands. The second part leads to the shift left and right from the direct transition, as can be seen from the resulting energy eigenvalues.

$$\epsilon_{\pm}(\mathbf{k}) = \frac{\hbar^2}{2m} k^2 \pm \alpha k \quad (3)$$

where

$\mathbf{k}$	electron wave vector
$m$	electron mass
$\alpha$	strength of the spin orbit coupling as defined in Eq.(2)

The degenerate parabolic bands are therefore shifted to the left and right in wavevector space which can also be seen in the band structure calculated by Brivio et al.[15] and depicted in a schematic in Fig. 4.

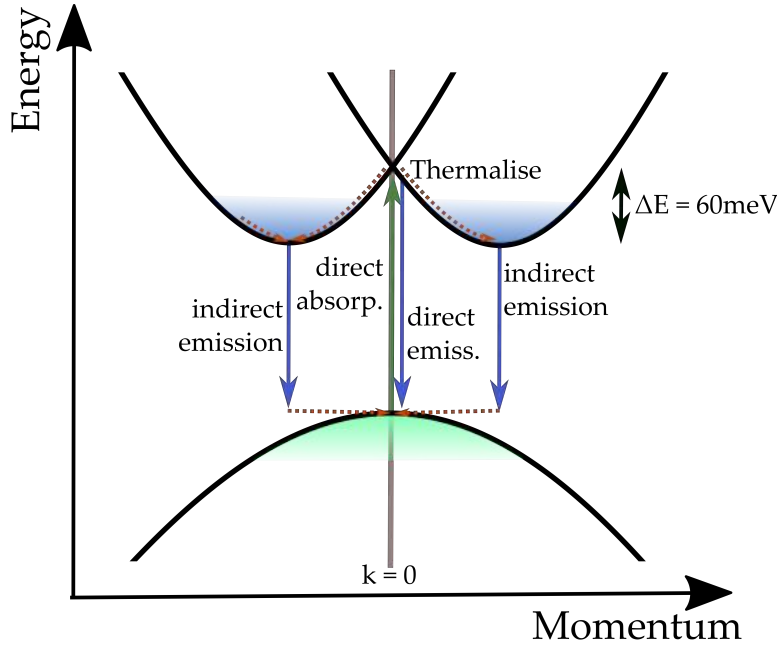


Figure 4: Schematics of the [MAPI](#) band structure, showing a split conduction band (mainly on the lead atom) and a valence band (mainly on the iodine atom)

In the following paragraphs I will show how this split of the conduction band can explain the [MAPI](#) properties of high absorption coefficients, typical for a direct semiconductor, and the long carrier lifetimes, typical for an indirect semiconductor.

**EFFECTS ON ABSORPTION** The absorption of photons in the above mentioned band structure can still happen without the need of a phonon. There is still a direct transition that is accessible by photons with energy higher than the (direct) bandgap energy. According to Fermi's golden rule, the density of states of both the starting and end states has to be high for a fast absorption. Since the valence band does not have a strong splitting, there are many states near  $k = 0$  available. Additionally, the energy difference between direct and indirect band-edge is small (60 meV), so there are still enough states available in the conduction band for the transition to occur. This means that an efficient absorption is possible despite the indirect transition being lower in energy. Weak absorption is also expected into the indirect band-edge, at photon energies 60 meV below the direct bandgap, as shown in chapter 4.

**EFFECTS ON CHARGE CARRIER LIFETIME** The long carrier lifetime can be explained by the indirect nature of the bandgap ([12]).

Most light is absorbed via the direct transition, the generated charge carriers quickly relax to the energetically lower bandedges left and right in wavevector space from the direct transition (see Fig. 4). The excess energy is lost through heat, i.e. phonons (Fig. 4). At the bandedges the electrons then need a phonon to recombine radiatively (by recombining with another charge carrier) or non-radiatively (by being trapped at a trap state). This makes the decay inefficient, resulting in a long lifetime. The lifetime should then depend on the spin orbit coupling strength and the electric potential gradient, both changing the split in momentum space. The phonon density of states influences the lifetime, because a higher number of phonons with the required momentum will render the decay more efficient.

### 1.3 EXPERIMENTAL METHODS

#### 1.3.1 *Sample preparation*

The [MAPI](#) samples were prepared by TianYi Wang. The lead iodide and the methylammonium iodide precursors were mixed and spin coated on a silica substrate. The samples were annealed on a hotplate which formed a dark brown film of around 300 nm thickness.

#### 1.3.2 *Pressure induced band structure change*

A small change in atomic distance leads to drastic changes in the wavefunction overlap of the orbitals around the atoms, which in turn changes the band structure. This behavior has been observed for other materials [16, 17]. The absorption, photoluminescence and charge carrier lifetime are investigated while the band structure changes under the application of pressure. This information can be used to find evidence for or against the hypothesis of an indirect bandgap.

I employ hydrostatic pressure experiments to change the crystal structure, which includes the distance of the lattice constant and possibly of sub-lattice tilting angles. The Young's modulus of [MAPI](#) is relatively low ( $\sim 20$  GPa, [18]), allowing for a change of  $\sim 2\%$  of the lattice constant at 400 MPa.

We use a ISS Llc pressure system. It contains the pressure cell, roughly 10cm wide, and a pressure generator in the form of a manual pump (Fig. 5). The pressure cell is filled with an inert pressure liquid: Ethanol, 3M Fluorinert FC43, or 3M Fluorinert FC72 used in this work. The pressure liquid transmits the pressure from the piston in the pump into the pressure cell. The pressure can be read off a manual gauge with an error of 20 MPa, as estimated from the experiment to experiment variation. We can access the sample optically through four sapphire windows. Simultaneous excitation and collec-

*Why do we use  
pressure?*

tion of light is possible. An electrical plug is available which allows for an electrical feed through. This plug was used in chapter 5.

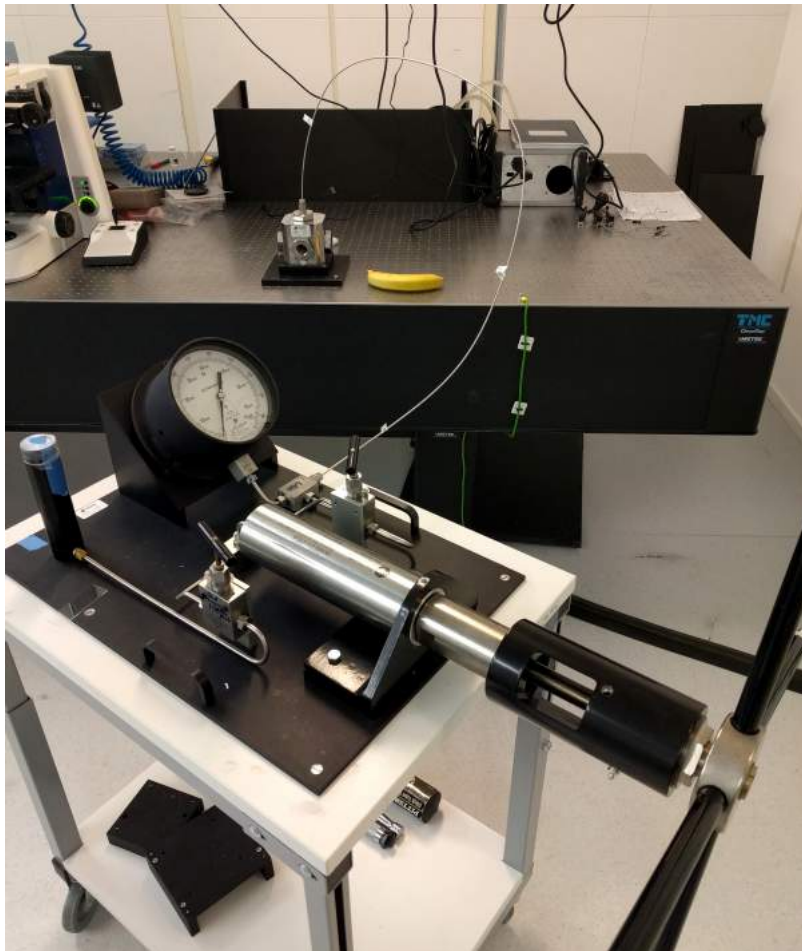


Figure 5: *Background:* Pressure cell from ISS LLC., with four windows for optical measurements and a plug on top that connects to a pressure tube used to transfer the Fluorinert FC-72 pressure liquid. Banana for scale. *Foreground:* manual pump with liquid reservoir, valves, and analog pressure gauge.

#### 1.4 STRUCTURE OF THIS WORK

This work contains three pressure measurement chapters and one data analysis chapter, structured as follows:

**FIRST** Steady state PL measurements under pressure are explained in Chapter 2, giving insight in the emission energy of MAPL.

**SECOND** The main part of this work is the measurement and analysis of transient PL data under pressure in Chapter 3, taken in a TCSPC setup.

**THIRD** The reanalysis of Photothermal Deflection Spectroscopy (PDS) absorbance data in Chapter 4, using the Tauc formalism.

**FOURTH** Resistance measurements under pressure, taken in the dark and under illumination in Chapter 5.

## PHOTOLUMINESCENCE SPECTRA UNDER PRESSURE

This chapter investigates pressure induced band structure changes in [MAPI](#) *via* steady state [PL](#). The energy of the [PL](#) peak is the energy of the bandgap, assuming negligible stark shift. The analysis of the [PL](#) spectrum under pressure opens a way to probe pressure induced changes in the band structure. The shape of the [PL](#) peak can contain additional information about the underlying processes that lead to radiative recombination.

### 2.1 METHODS

A laser with a wavelength of 640 nm (PicoQuant LDH-D-C-640) and a power of 0.7 mW was focused on a thin sample of [MAPI](#), tilted at 45°. The laser light was filtered out of the detection path with two Thorlabs FEL-700 highpass filters and then focused into a fiber by a lens. The fiber was connected to a OCEANVIEW USB4000 spectrometer. The setup was integrated into the [TCSPC](#)-setup used in chapter [3](#) and seen in [Fig. 11](#). The pressure was varied throughout the experiment, from 0 MPa to 400 MPa. The experiment and analysis was conducted in collaboration with TianYi Wang, fitting of the data was done by TianYi Wang.

### 2.2 RESULTS

Three spectra at different pressures are shown in [Fig. 6](#). A fit of the data is included. Two Voigt profiles<sup>1</sup> are needed to describe the data. The main peak at around 1.61 eV is assigned to the direct bandgap transition, whereas the side peak at 1.55 eV is assigned to the indirect transition from the bandedge to the valence band. The whole band structure changes, with the bandgap of direct *and* indirect transition becoming smaller over pressure, up to a phase transition at 320 MPa where it increases abruptly. The phase transition is from tetragonals (< 320 MPa) to cubic [[19](#)] or orthorombic [[20](#)] (> 320 MPa).

The energy distance between main and side peak is 60 meV, as predicted by theory [[11](#)]. The area of the side peak in comparison to the main peak becomes larger under pressure ([Fig. 6](#) and the yellow data points in [Fig. 7](#)). After the phase transition at a pressure of 320 MPa

<sup>1</sup> A Voigt profile is the convolution of a Gaussian and a Lorentzian probability distribution, and was found to describe the line shape most accurately



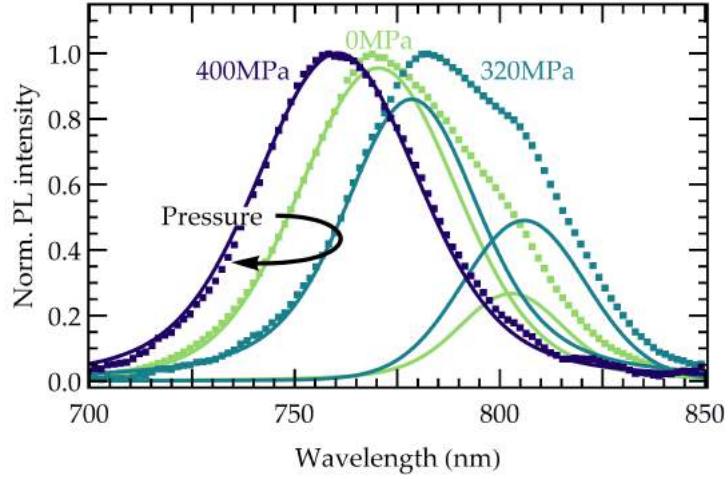


Figure 6: PL spectra and fits at three different pressures. At pressures below phase transition (320 MPa) the PL fit requires two peaks while above the phase transition only one peak suffices.

only one peak is sufficient to fit the data, as seen in the dataset at 400 MPa.

### 2.3 DISCUSSION

*Whats the origin of the side peak?*

The decreasing side peak can be understood by proposing a decreasing Rashba split parameter  $\alpha$  with pressure. Pressure could lead to an alignment of the MA dipoles, reducing the net electric field. Another mechanism could be reduced lattice tilting at higher pressures that would make the crystal more centrosymmetric, thus reducing the net electric field acting on the led site<sup>2</sup>. If the high pressure phase above 320 MPa is in fact cubic (as measured by [19]), this could explain the lack of indirect transition<sup>3</sup> in this phase. A cubic crystal is centrosymmetric and cannot have the internal electric fields necessary for Rashba splitting.

**DECREASING RASHBA SPLIT** If the Rashba splitting decreases with pressure the two parabolic bands left and right from the direct transition are expected to move closer to  $k = 0$  (depicted in Fig. 8). Then the energy difference between direct (main), and indirect (side) peaks should also become smaller over pressure. In Fig. 9 we can see that the distance in energy decreases from 61 meV to 53 meV. This trend is consistent with our expectations; a quantitative comparison with theory was not attempted.

<sup>2</sup> A combination of both effects is also possible

<sup>3</sup> lack of side peak



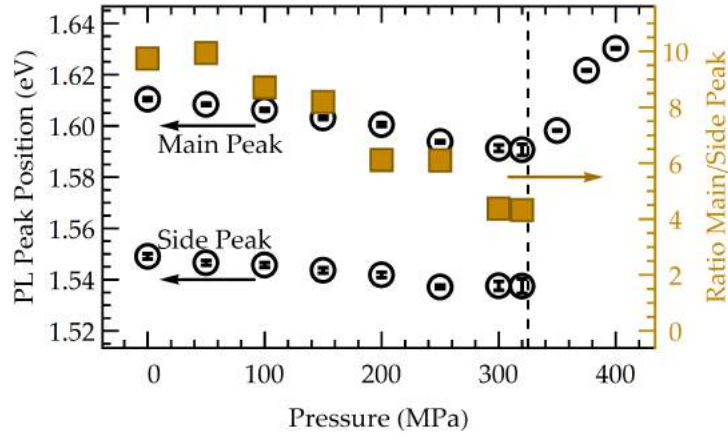


Figure 7: Position of main and side peak as extracted from fit to PL data. The ratio of main to side peak intensity decreases with rising pressure. Black bars represent error bars derived from the fit error.

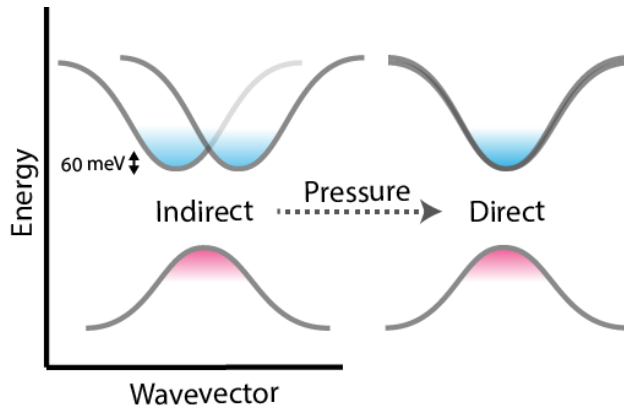


Figure 8: Increasing pressure leads to a decrease in Rashba splitting, making the bandstructure more direct.

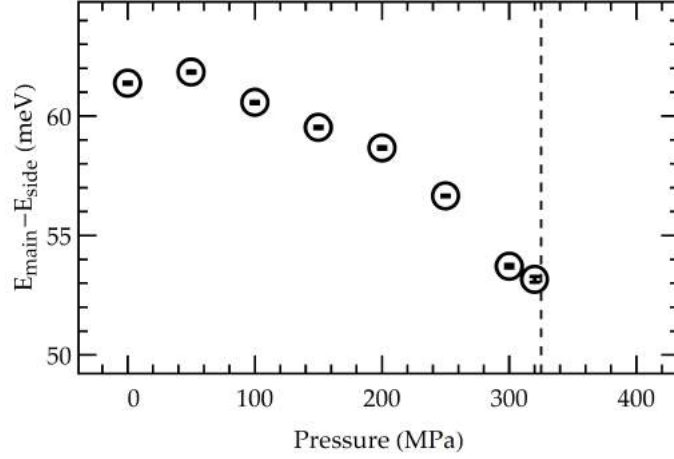


Figure 9: Decreasing peak position difference of main to side peaks over pressure, consistent with the hypothesis of smaller Rashba splitting at high pressure. Black bars represent error bars derived from the fit error.

**DISAPPEARING SIDE PEAK AT HIGH EXCITATION DENSITIES** At high excitation densities the bands are filled with charge carriers [12], which makes the faster direct transition (60 meV above the indirect band edge) the dominant decay channel. We see this behavior recovered in our experiment. Fig. 10 shows the PL at two different charge carrier densities. The high charge carrier density peak shows a blue shift through Burstein–Moss band filling [21] and has no side peak contribution.

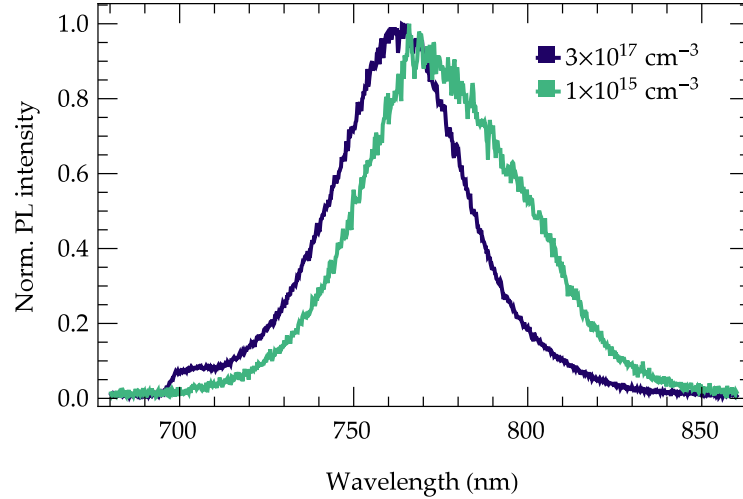


Figure 10: Transition between low and high excitation power regime shows a disappearing side peak as expected from theory. The blue shift is likely a result of band filling.

## 2.4 COMPETING EXPLANATIONS

In the following I want to explore other theories that might explain the presence of the side peak.

**PHONON ASSISTED RECOMBINATION** The side peak could also be explained by a direct bandgap and a phonon assisted recombination. This means that the charge carrier that relaxed thermally to the bandedge absorbs a phonon and then is able to decay from an energetically higher point in the band structure. Therefore this transition has a larger distance in energy, meaning the photon emitted has a larger energy. This is not the case in our experiment, rendering this explanation unlikely. Additionally, we have to note that the side peak is very localized at 60 meV below the main peak. The explanation of electron phonon scattering with a phonon of exactly 60 meV is possible but in reality not the case. There is no distinct feature in the Raman scattering spectrum at this energy, rather there are many at different energies [15].

**TRAP ASSISTED RECOMBINATION** Wetzelaer et al. find dark trap states to be the dominant decay mechanism of charge carriers in [MAPI](#). Measurements of the [MAPI](#) diode ideality factors assert that the traps are dark, e. g. that they do not emit photons upon charge carrier trapping [22]. It is therefore unlikely that our side peak is caused by a new type of radiative trap.



## TRANSIENT PHOTOLUMINESCENCE OF MAPI UNDER PRESSURE

---

The MAPI sample sits in the pressure cell, which allows a change of hydrostatic pressure. Pressure induced bandstructure changes affect charge carrier lifetime. As seen in chapter 2, we expect a decrease of Rashba splitting with pressure which consequently affects charge carrier lifetime. The analysis employed allows for the extraction of radiative and non-radiative decay rates and the fraction of charge carriers decayed through either channel. The fraction of radiatively decayed charge carriers is a measure proportional to the radiative efficiency.

### 3.1 GENERAL WORKING TECHNIQUES OF TCSPC

In Chapter 2 the sample was excited by a continuous laser beam, which supplies the steady state response of the system. By exciting the sample for a short period of time with a laser pulse the subsequent PL decay is accessible for detection. If this decay would be slow ( $\sim$  ms regime) a simple photodiode would suffice to measure the temporal PL decay. However, the decay of charge carriers in MAPI is in the  $\sim$  ns range which makes this method inapplicable. TCSPC is a solution for measuring on such short time scales. One pulse of laser light hits the sample, inducing charge carriers in the material, which then recombine and emit photons. The delay of PL-photon detection with respect to the excitation pulse is recorded<sup>1</sup> and counted in a histogram.

*Why do we have to use TCSPC?*

The working principle of TCSPC is that the excitation is very weak, so that only in about 1%<sup>2</sup> of the excitation pulses there is a photon emitted from the sample. The result is that during one excitation cycle only one single photon or no photon is detected<sup>3</sup>. Repeating the excitation cycles for a few thousand times allows for the creation of a histogram with time on the x axis and the counted photons in a respective time bin on the y axis. This histogram represents the temporal decay of the PL-signal.

---

<sup>1</sup> this is where the "time correlated" in the name stems from

<sup>2</sup> this prevents the so called pile-up effect, that occurs because the detectors have a deadtime after the detection of a photon in which they are insensitive to an arriving second photon

<sup>3</sup> This is where "single photon" in the name stems from

## 3.2 MEASUREMENT PROCEDURE

A picture of our setup can be seen in Fig. 11.

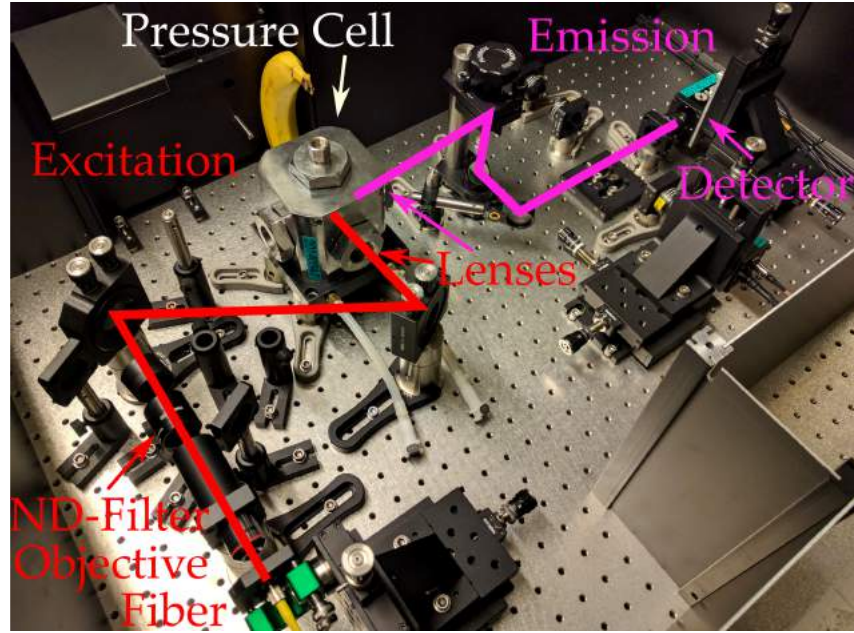


Figure 11: Picture of the TCSPC setup, showing the outcoupling of the 640 nm laser into a objective on the left bottom, OD filters for power control, the pressure cell with optics attached and the detector. Banana for scale.

We measured on a home-built setup equipped with

LASER DRIVER PicoQuant PDL 828 "Sepia II"

EVENT TIMER PicoQuant HydraHarp 400

LASER HEAD PicoQuant LDH-D-C-640

PHOTON DETECTOR Micro Photon Devices, MPD-5CTD

Decay curves at different hydrostatic pressures were taken by increasing the pressure in 50 MPa steps <sup>4</sup> and waiting 7 min in between measurements. This time was needed so that the pressure cell and sample could respond to the high pressures. The laser was blocked in between measurements. After the highest pressure point at 400 MPa the pressure was released with the same waiting time in between pressure steps. Measuring the up and down strokes served as a check for the reversibility of the transient PL signal from MAPI under pressure, and consequently for the reversibility of the band structure changes.

<sup>4</sup> 10 MPa steps near the phase transition

**INSTRUMENT RESPONSE FUNCTION** The excitation pulse is not a delta function, it has a certain width. The fiber and the detector add to this temporal uncertainty. All these effects combined are called the Instrument Response Function (IRF) (see Fig. 12) The IRF is measured

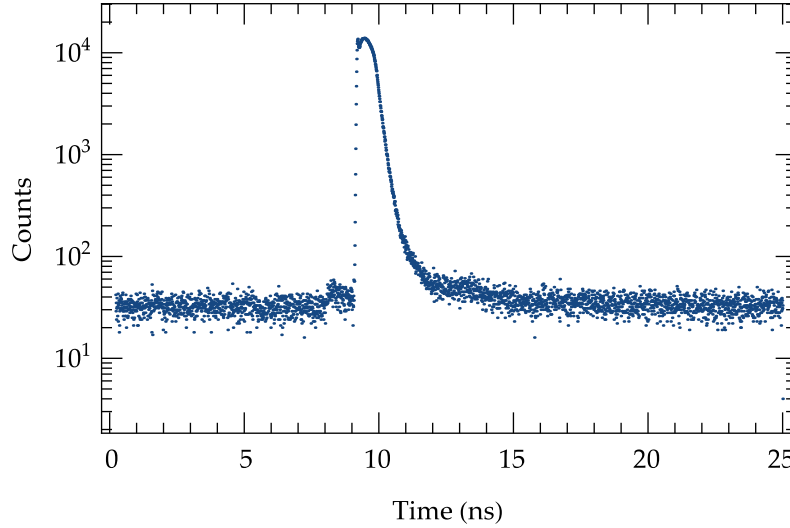


Figure 12: The IRF of our system, taken via scattering of the laser by a dilute solution of ZnO. The timescale of  $\sim$  ns is much faster than the MAPI decay.

by using a dilute solution of ZnO nanoparticles with size  $< 130$  nm that scatter heavily. The scattering allows for a direct measurement of the temporal instrument response, at a wavelength of 640 nm. It would be better to use an ultra-fast fluorophore that instantaneously emits at the MAPI PL wavelength to account for the spectral response of the detector, but we did not have such a fluorophore and the wavelengths did not differ too much.

*Is the setup fast enough?*

The spectral response from the specification sheet of the detector shows that the response is sufficiently flat. I account for the IRF by analyzing only temporal data after 1 ns after the start of the decay, which is the Full Width at Half Maximum (FWHM) of the IRF.

### 3.3 MEASUREMENT DATA

Raw data of the measurement is shown in Fig. 13. The decay becomes faster at higher pressures, meaning that the charge carriers are shorter-lived at high pressures.

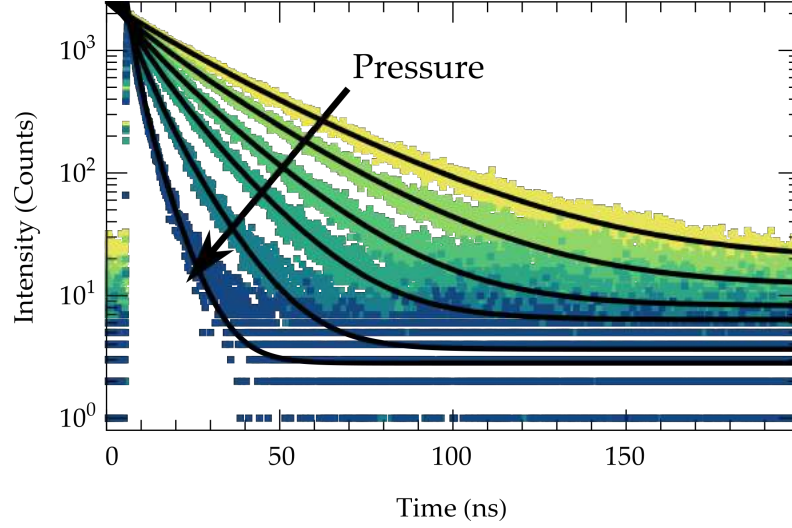


Figure 13: Raw data with fit of the decays at different pressures of pressure down stroke, showing a faster decay at higher pressures and comparable starting height. Fit and data shows good agreement. Pressures down stroke data shown at pressures from light green to dark blue: 0 MPa, 50 MPa, 100 MPa, 150 MPa, 235 MPa, 350 MPa

### 3.4 MODEL TO DESCRIBE DATA

I fit the data to a simple two process model to extract quantitative information from the raw decay curves. The model describes the charge carrier density change over time.

*How can we understand the decays?*

$$\frac{dn(t)}{dt} = -\underbrace{k_R n(t)^2}_{\text{bi-mol.}} - \underbrace{k_{NR} n(t)}_{\text{mono-mol.}} \quad (4)$$

$$n(t=0) \equiv n_0 \quad (5)$$

where

- $\frac{dn(t)}{dt}$  change of charge carrier density over time
- $n(t)$  charge carrier density
- $k_R$  radiative decay rate
- $k_{NR}$  non-radiative decay rate
- $n_0$  initial charge carrier density

The formula has a bi-molecular part, describing two charge carriers that recombine radiatively and a mono-molecular part that describes the decay of a single charge carrier non-radiatively. It is not *a-priori* clear that the mono-molecular is non-radiative; however, Wetzelaer et al. has shown by analyzing the ideality factors of the MAPI "diodes" that the trap states decay non-radiatively [22]. To use this line of reasoning, we have to assume that the monomolecular decay is governed



by these trap states, which is reasonable since Wetzelaer et al. also showed that the main decay channel is through these dark trap states. The bi-molecular recombination is mostly radiative [22]. This model is already used for the analysis of temporal data of MAPI [23].

**SOLUTION FOR PARTS OF THE DECAY FORMULA** If we solve only one part of eq. (4) for  $n(t)$  we get different curve shapes. This allows us to distinguish between them reliably by fitting the data to the model.

DECAY CHANNEL		PART OF FORMULA	SOLUTION
bi-molecular	radiative	$\frac{dn(t)}{dt} = -k_R n(t)^2 \Rightarrow$	$n(t) = \frac{1}{k_R t + 1}$
mono-molecular	non-radiative	$\frac{dn(t)}{dt} = -k_{NR} n(t) \Rightarrow$	$n(t) = \exp(-k_{NR} t)$

Table 1: Solution of individual parts of Eq. (4) with solution

as we see from Table 1 only the mono-molecular part decays exponentially. It is therefore wrong to just fit an arbitrary number of exponential decays onto the data and then assigning them to various decay processes. The whole solution of Eq. (4) with contributions from *both* decay channels is shown in Eq. (6). The derivation is using the boundary condition of a constant initial charge carrier density seen in Eq. (5).

$$n(t) = \frac{k_{NR} n_0}{(k_{NR} + n_0 k_R) \exp(k_{NR} t) - n_0 k_R} \quad (6)$$

The PL-signal is proportional to  $n^2$ , under the assumption that only the bi-molecular process leads to the emission of a photon.

$$PL(t) = A_0 \cdot n(t)^2 + C \quad (7)$$

The formula (7) includes a proportionality factor  $A_0$  that contains the detection efficiency, and a constant background term  $C$ . This formula describes our observable, the PL intensity over time.

### 3.5 FITTING PROCEDURE

Formula (7) has to be fitted to the measured PL curves in Fig. 13. To do so, I absorb the initial charge carrier density  $n_0^2$  and the proportionality factor  $A_0$  into a new proportionality factor  $A$ . I absorb  $n_0$  and  $k_R$

into  $k_R^0$ , since both are highly correlated, and therefore it would be a poor choice of parameters to fit both.

$$n(t) = \frac{k_{NR}n_0}{(k_{NR} + n_0k_R) \exp(k_{NR}t) - n_0k_R} \quad (8)$$

$$= n_0 \left( \frac{k_{NR}}{(k_{NR} + k_R^0) \exp(k_{NR}t) - k_R^0} \right) \quad (9)$$

$$\Rightarrow PL(t) = A_0 \cdot n(t)^2 + C \quad (10)$$

$$= \frac{A_0 k_{NR}^2 n_0^2}{((k_{NR} + n_0k_R) \exp(k_{NR}t) - n_0k_R)^2} + C \quad (11)$$

$$= \frac{A k_{NR}^2}{((k_{NR} + k_R^0) \exp(k_{NR}t) - k_R^0)^2} + C \quad (12)$$

There are four parameters left that have to be determined by the fitting algorithm.

The background can be calculated by taking the average of the first measurement points before the laser pulse hits the sample. Doing so eliminates one fitting parameter. From the three remaining parameters only the rates are interesting, since  $A$  is just a normalization factor representing the counts at the beginning of the decay.

The counting of photons is subject to the Possonian error  $\delta N_i = \sqrt{N_i}$ , where  $N_i$  is the count number in bin  $i$ . The algorithm weighs each data point with  $\frac{1}{\delta N_i^2}$  with the counting error  $\delta N_i = \sqrt{N_i}$ , resulting in the weighing factor:

$$\omega_i = \frac{1}{N_i} \quad \forall N_i > 0 \quad (13)$$

This procedure was implemented into the `MATHEMATICA` function `NonlinearModelfit`, which uses a minimization of the mean root square measure to find the best fit. This procedure is questionable since it assumes an underlying normal distribution of the measured values around an unknown "real" value. As we have seen before the distribution of the errors is in fact Possonian if counting data is concerned. The correct way to implement this underlying error distribution is to numerically maximize a Maximum Likelihood estimator including a Possonian probability density function. Doing so was attempted but ultimately not successful due to time constraints. However, we can exploit the fact that a Possonian distribution converges to a Normal distribution if the mean value is high enough. If we only use the data above a sufficiently high count number, the data is approximately normally distributed around the mean. Usually a mean of 10 is seen as sufficient to make this approximation. The background is the only significant signal in this low count rate regime. Since we already determined the background we do not have to fit it and thus

lose no information by only fitting the "high" count rate regime. I implemented this procedure in a cutoff function that crudely fits an exponential decay to the data and extracts the time where the signal reaches ( $N_{\text{background}} + 15$ ) counts .

The extracted time is then used as a boundary to fit the data to formula (12). The resulting fits for the pressure up stroke are shown in Fig. 13.

**GOODNESS OF FIT** The standard method of assessing the quality of a fit is the reduced chi-squared ( $\chi_{\text{red}}^2$ ) measure, which calculates the mean root distance from the data points to the fitted curve, normalized by the standard deviation. A perfect fit has  $\chi_{\text{red}}^2 = 1$ , whereas an over-fit<sup>5</sup> has a value of  $\chi_{\text{red}}^2 < 1$  and a poor fit<sup>5</sup> has  $\chi_{\text{red}}^2 > 1$ . However, how close  $\chi_{\text{red}}^2$  has to be to unity is open to debate and is ultimately indeterminable.

The  $\chi_{\text{red}}^2$  measure also assumes a normal distribution of the data, an important constraint that has to be considered. Since our measurement data should be approximately normally distributed after the above discussed treatment, this is not hindering the applicability of the  $\chi_{\text{red}}^2$ -test.

However, there is a fundamental concern on the validity of the  $\chi_{\text{red}}^2$ -Test. As Andrae, Schulze-Hartung, and Melchior show, the  $\chi_{\text{red}}^2$ -Test must only be used in linear models with independent free parameters [24]. Even then the value of  $\chi_{\text{red}}^2$  is subject to noise, which can be significant and reduces the confidence in a chosen cutoff value even further. Andrae, Schulze-Hartung, and Melchior make it clear that in a highly non-linear model such as the one I seek to use in this analysis, the degrees of freedom are ill-defined, rendering the method useless. Several alternative goodness of fit measures are proposed, such as bootstrapping, leave one out validation, and normality of the residuals. The last is the most straightforward to analyze, and is implemented in the fitting algorithm in this work. The standardized residuals are analyzed by a Cramer-von Mises test, a strong test for normality. The null hypothesis of this test is that the residuals are normally distributed. The first cutoff criteria of a good fit is whether or not this null hypothesis can be rejected on the 5% significance level. This significance level is arbitrary and cannot be considered a bright line of decision making, as pointed out recently by the American Statistical Association [25]. Fig. 14 shows the P-values of all fits, with all but three being above the significance level. If the P-value is below the 5% level more information about the experiment and closer examination is needed to draw conclusions about the rejection of the null

*How can we assess our fit?*

<sup>5</sup> An over-fit is created if the model has too many free parameters; limiting the value of the fit. A poor fit means the model cannot accurately describe the data.

hypothesis. Fig. 15 shows the residuals of the three fits with  $P < 0.05$  and corresponding histograms. There is no structure visible, which would indicate a poor fit, allowing us to accept these fits as sound.

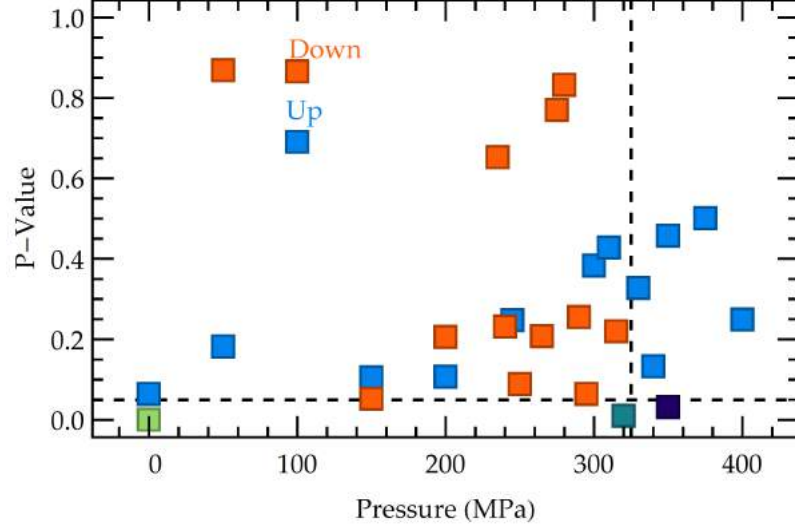


Figure 14: P-Values of Cramer-von Mises test of residuals ( $P < 0.05$  in colors corresponding to Fig. 15)

We can conclude that the fitting algorithm is very strong - it has only two fitting parameters that describe the data accurately, with the quality of the fit assessed by a statistically sound method.

### 3.6 EXTRACTION OF DECAY PATH IMPORTANCE

From the fit of the model to the data the radiative and non-radiative rates can be extracted, as seen in Fig. 16.

**COMPARISON WITH LITERATURE VALUES FOR THE RATE CONSTANTS** Wehrenfennig et al. carried out a measurement of the rate constants at ambient pressure on films of the same material using THz techniques [26]. We compare this with our measurement at 0 MPa. Wehrenfennig et al. measured at charge carrier densities of  $10^{17} - 10^{19} \text{ cm}^{-3}$ , considerably higher than our density of  $10^{14} \text{ cm}^{-3}$  (calculated in Sec. 3.8). They reported a non-radiative recombination rate of  $14 \mu\text{s}^{-1}$ , whereas we measure  $(20.0 \pm 0.2) \mu\text{s}^{-1}$ , with the error derived from the fit. They report a radiative recombination rate of  $k_R^{\text{lit}} = 9.2 \cdot 10^{-10} \text{ cm}^3 \text{ s}^{-1}$ . Our calculation is using an initial charge carrier density of unity ( $1 \text{ cm}^{-3}$ ). Therefore  $k_R = \frac{k_R^0}{n_0}$  here having the value of  $(1.85 \pm 0.05) \cdot 10^{-8} \text{ cm}^3 \text{ s}^{-1}$ , is around 20 times higher than reported by Wehrenfennig et al. The vastly different excitation densities [26],

*Are our values  
reasonable?*

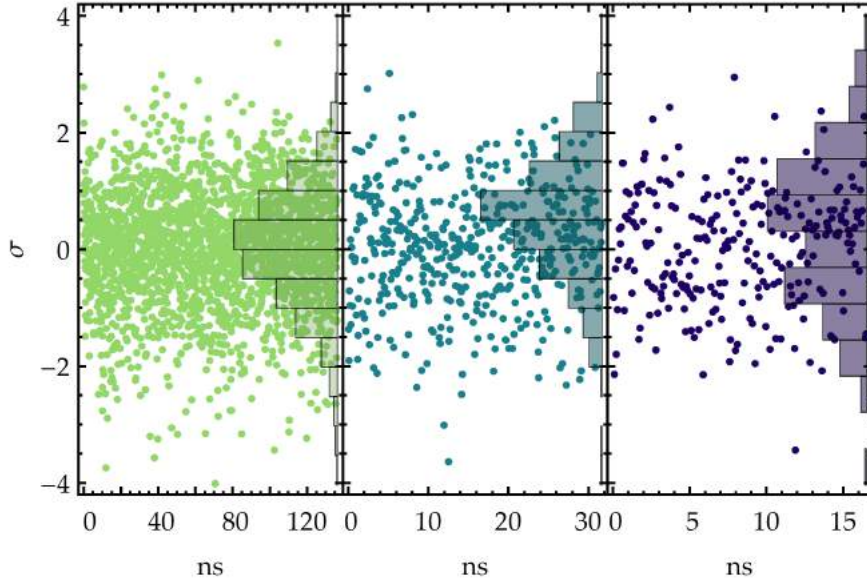


Figure 15: Residuals of fits with  $P < 0.05$  from Fig. 14. Deviation from normal distribution is visible, leading to small P-values. The residuals show no structure, meaning the fit can be accepted.

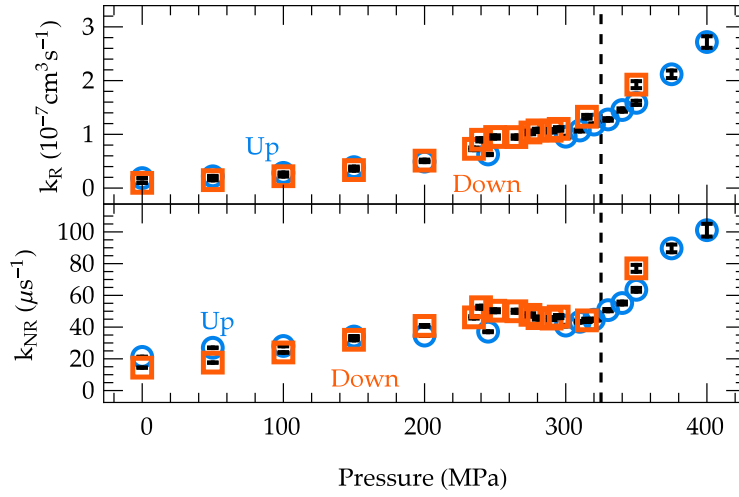


Figure 16: Radiative ( $k_R$ ) and non-radiative ( $k_{NR}$ ) rates extracted from the fit, increasing drastically with pressure. Black bars represent error bars derived from the fit error.

as well as the different techniques (TCSPC vs. THz photoconductivity measurements) and batch-to-batch variations might explain the difference.

### 3.6.1 Ratio of decay paths

A direct comparison between radiative and non-radiative decay rates is invalid, since the units are different. This case is different from the steady-state case, where the charge carrier density is constant. In this case the direct calculation of the PL-quantum yield is possible by taking the ratio of radiative rate to all decay rates [27].

*Which path is more important?*

We can however, compute the amount of charge carriers decayed through either channel, in relation to the total amount of charge carriers decayed. This procedure is shown as follows.

Integrating the two parts of Eq. (4) over time and normalizing to the total decayed charge carriers yields the portion of charge carriers decayed through one of the channels. The radiative part (Eq. (14)) is the "internal" photoluminescence quantum yield, representing the efficiency of converting an electron-hole pair into a photon. The PL quantum yield is the "internal" quantum yield multiplied with an out-coupling efficiency.

$$\Theta_{\text{Rad}} = \frac{\int_{t=0}^{\infty} k_R n(t')^2 dt'}{\int_{t=0}^{\infty} k_R n(t')^2 + k_{NR} n(t') dt'} \quad (14)$$

$$\Theta_{\text{Non-Rad}} = \frac{\int_{t=0}^{\infty} k_{NR} n(t') dt'}{\int_{t=0}^{\infty} k_R n(t')^2 + k_{NR} n(t') dt'} \quad (15)$$

The result is plotted in Fig.17.

The decay becomes more radiative over pressure, meaning that the decay process becomes more efficient. This corroborates that traps are not responsible for the side peak seen in the PL data. The side peak is stronger at higher pressure, which should render the decay less efficient if caused by radiative traps.

## 3.7 JUSTIFICATION OF ASSUMPTIONS IN MODEL

The model described above makes certain assumptions. We assume that there is no considerable Auger process present. Electron and holes are treated as free charge carriers, and their initial density upon excitation is assumed to be constant. These assumptions will be justified in the following subsections. I present additional insight into

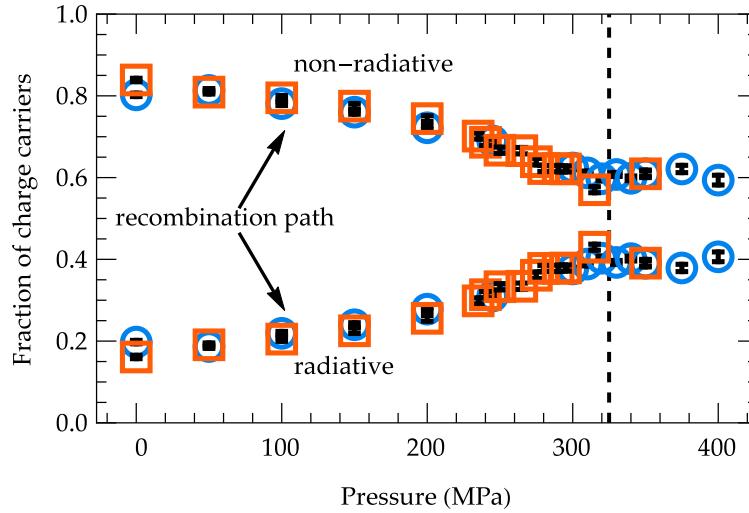


Figure 17: Fraction of radiatively and non-radiatively decayed charge carriers as shown in Eq. (14) and Eq. (15). Black bars represent error bars. The errors are derived from a Gaussian error propagation of Eq. (14) assuming independent parameter errors. Parameter errors are from the fitting algorithm.

the effect of a changing initial charge carrier density on the fitting algorithm and an extension of the model to accommodate for this case.

### 3.7.1 Auger term

The model explained above has no Auger term; only mono- and bi-molecular recombination is considered. Auger recombination happens if an electron-hole pair recombines and transfers its energy to another electron. Three charge carriers have to interact for this process to happen, hence only at high charge carrier densities can significant portions of the charge carriers decay via Auger recombination. To verify this assumption, I took transient PL data at ambient pressures with one order of magnitude more laser power than in the pressure experiment, and varied the laser power in this range. The Auger recombination should then be present in the first nanoseconds upon excitation since Auger recombination is a fast process. It is also expected to be very intensity dependent, scaling with the charge carrier density cubed. The data is shown in Fig. 18. No additional intensity dependent decay is visible. Following Occam's razor principle<sup>6</sup> we should therefore abstain from introducing a third, unnecessary parameter.

*Can we really neglect Auger recombination?*

<sup>6</sup> "Among competing hypotheses, the one with the fewest assumptions should be selected."

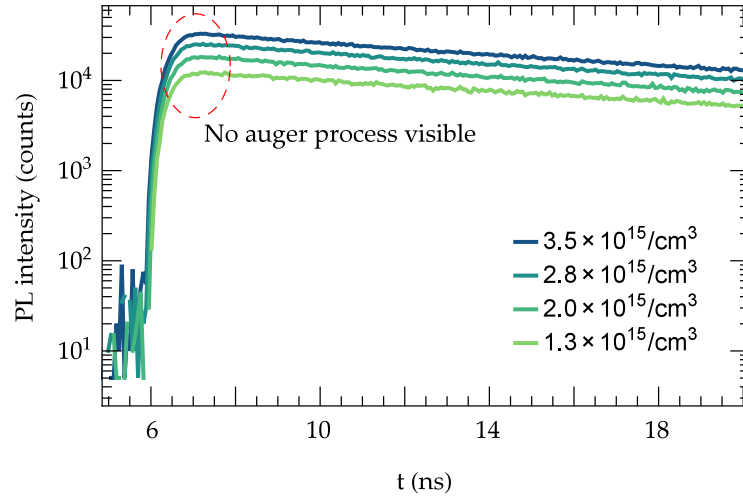


Figure 18: Check for the absence of an Auger-term. Increasing the charge carrier density leads to no additional fast decay component.

### 3.7.2 Treatment of electrons and holes as charge carriers

A semiconductor creates an electron-hole pair after absorption of a photon. In the treatment above both are considered indistinguishable and treated as free charge carriers. This is an approximation and one requirement for this to be valid are comparable mobilities of both species. This condition is met in MAPI with a mobility of  $5 - 10 \text{ cm}^2 \text{ V}^{-1} \text{ s}^{-1}$  for holes and  $1 - 5 \text{ cm}^2 \text{ V}^{-1} \text{ s}^{-1}$  for electrons [28]. The absence of excitons is discussed in chapter 1.

This assumption is commonly done in the field, as seen in a review paper by Herz [6].

### 3.7.3 Photodiode test

Is  $n_0$  constant?

The model above assumes a constant  $n_0$  across the pressure measurement as only then is it possible to absorb  $n_0$  and  $k_R$  into  $k_R^0$ . The used pressure liquid Fluorinert FC-72 becomes slightly milky at around 200 MPa and above, which could lead to a different laser power hitting the sample. The additional scattering could in turn lead to a different initial charge carrier density  $n_0$ . To quantify this influence I placed a silicon photodiode, encapsulated in plastic, in the pressure cell and measured the incident light intensity, upon constant illumination by a white Thorlabs Light Emitting Diode (LED). The result can be seen in Fig. 19. The variation stays below 5% making the assumption of constant illumination sound.



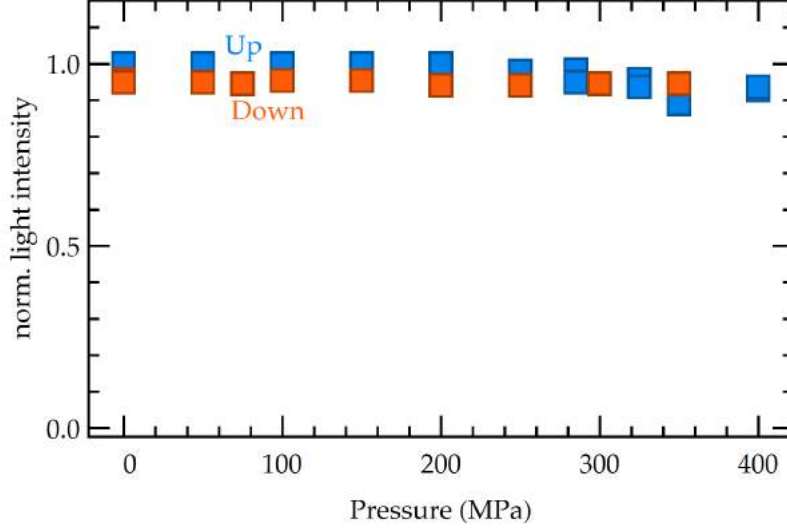


Figure 19: Light intensity in pressure cell with changing pressure to assess changes in opacity of the pressure liquid. A silicon photodiode in the pressure chamber measures the photocurrent. Light intensity measured by driving voltage of LED-Driver necessary for 25  $\mu$ A photocurrent. Driving voltage and light intensity obey a linear relationship, as confirmed in a separate measurement.

#### 3.7.4 Initial charge carrier density influence

Despite having shown that the light power incident on the [MAPI](#) sample is constant (Sec. [3.7.3](#)), I want to analyze the influence of a change in charge carrier density on the decay dynamics.

Since the radiative and non-radiative decay channels scale differently with  $n$  ( $\propto n^2$  and  $\propto n$  respectively) larger  $n$  leads to a faster decay upon excitation (Fig. [20](#)).

The similar shape of a decay taken at higher excitation energies and one with intrinsically faster radiative decay could lead to errors in the fitting. The faster decay at the beginning of the high  $n$  curves in Fig. [20](#) could be mistaken for a higher radiative decay rate.

The ratio of radiatively decayed charge carriers  $\Theta_{Rad}$  (Eq. [\(14\)](#)) increases with increasing  $n$  (limit seen in Eq. [\(16\)](#)). The non-radiative, linear term in the denominator is dominated by the radiative term, which is proportional to  $n^2$ .

$$\lim_{n \rightarrow \infty} \Theta_{Rad} = \lim_{n \rightarrow \infty} \frac{\int_{t=0}^{\infty} k_R n(t')^2 dt'}{\int_{t=0}^{\infty} k_R n(t')^2 + k_{NR} n(t') dt'} = 1 \quad (16)$$

To test whether the data taken under high pressure can be explained by an increasing  $n$  with pressure I fit the data taken at different excitation powers with our model that assumes constant excitation power. The result is seen in Fig. [21](#).

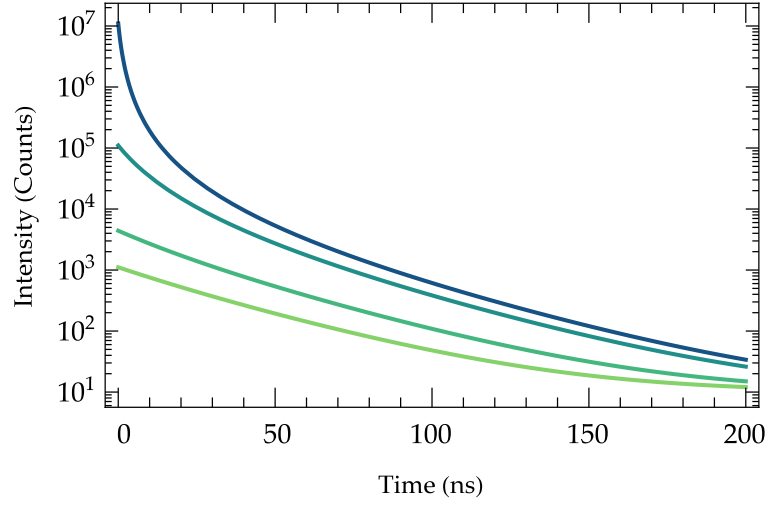


Figure 20: Theoretic curves of changing Charge carrier density  $n_0$  with constant  $k_R$  and  $k_{NR}$  taken from the ambient pressure data fit.  $n_0$  is increasing from light green to dark blue in steps of  $n_0 = \{1, 2, 10, 100\}$

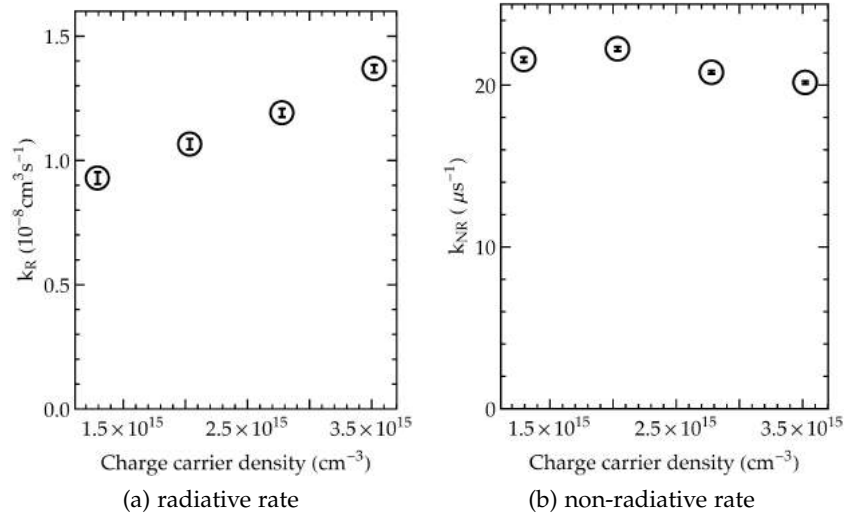


Figure 21: Change of  $k_R$  and  $k_{NR}$  with excitation density. The model assumes constant excitation energy which forces the algorithm to increase  $k_R$  to find the best fit. Black bars represent error bars derived from the fit error.

The algorithm increases the radiative rate to account for the faster decay, whereas the non-radiative rate is not affected by the change in excitation energy. This is different from the trend in our pressure measurement, and since the variation in excitation is much larger than the change detected by the photodiode (see section 3.7.3), changing charge carriers can be excluded as an explanation for an increasing radiative efficiency in the pressure measurement.

### 3.7.5 Global fit

This section shows the power of our model and confirms the independence of the rates on the excitation energy.

The data taken at different excitation fluxes and under ambient pressure (Fig. 18) is fitted with Eq. (4). Instead of absorbing  $n_0$  and  $k_R$  into  $k_R^0$  and fitting this parameter, both the radiative and non-radiative rates are set to the values extracted from the pressure experiment data at ambient pressures. I assumed that the initial charge carrier density  $n_0$  depends linearly on the laser power setting<sup>7</sup>, and used a *global* linear fit to extract the relationship between  $n_0$  and laser power. The result is seen in Fig. 22. The fit is not as good as in the pressure measurement but the important features are still captured. The discrepancy probably stems mainly from the constant radiative and non-radiative rates that were measured on a different day than the data in Fig. 18, leading to possible minor changes of the material. Also, the assumption of a linear relationship between laser power and initial charge carrier density  $n_0$  maybe not be entirely valid.

*Can we extend the model?*

## 3.8 CHARGE CARRIER DENSITY CALCULATION

To extract the real radiative rate  $k_R$  we have to calculate  $k_R = \frac{k_R^0}{n_0}$  meaning that we have to know the charge carrier density in the material. To calculate the charge carrier density we placed a power meter at the same position as our film inside the pressure cell and extracted a total power of 37  $\mu W$ . To calculate the power density, we replace the power meter with a beam profiler (Thorlabs BC106N-VIS/M, Fig. 23). We measure a peak power density of 62  $mW cm^{-2}$ , at which we observe a radiative efficiency of 20% at ambient pressure. This is in agreement with a PL quantum efficiency of <40 % at fluences of around 50  $mW cm^{-2}$  reported previously [29].

<sup>7</sup> The laser power setting is linear with laser power as a measurement with a power meter confirms

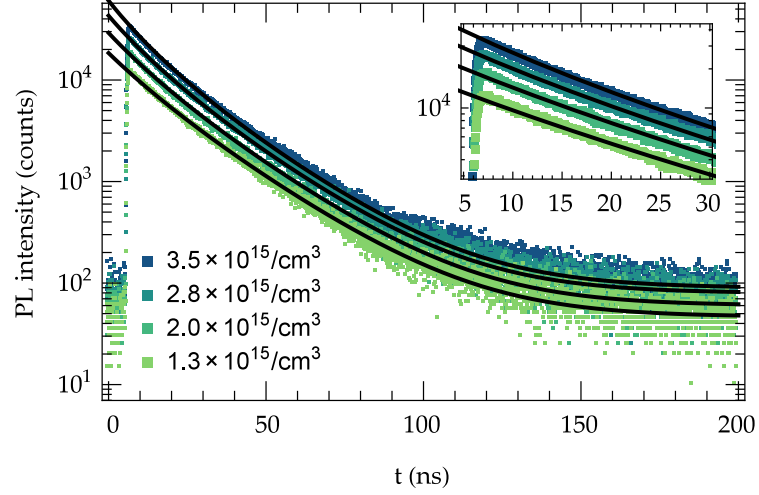


Figure 22: Global fit of high charge carrier density data with Eq. (12) and  $n_0$  as fit parameter. Constant  $k_R$  and  $k_{NR}$  are supplied from 0 MPa pressure measurement.  $n_0$  is assumed to depend linearly on laser power setting. Good agreement is achieved.

The repetition rate of excitation is 5 MHz, resulting in a excitation energy of  $12.4 \text{ nJ cm}^{-2}$  per pulse. To calculate the charge carrier density we used:

$$n_0 = \frac{\text{PowerDensity} \cdot \text{Absorbance}(640\text{nm})}{E_{\text{photon}}(640\text{nm}) \cdot d_{\text{sample}}} \cdot \text{geometry factor} \quad (17)$$

where

$n_0$	initial charge carrier density
PowerDensity	measured laser power density
Absorbance	absorbance of MAPI at 640 nm
$d_{\text{sample}}$	thickness of the sample (400 nm)
geometry factor	factor accounting for liquid and angle

The geometry factor accounts for the additional refraction because we measured the beam profile in air and not in liquid as in the pressure experiment, and the fact that we measured at  $45^\circ$  sample to beam orientation. For the calculation of the geometry factor the beam is first propagated until it hits the silica window where the size can be calculated from the distance and the focal length of the lens. The beam is then refracted twice, once at the air-silica and then at the silica-liquid interface. The beam is then propagated to the sample, where the beam radius is calculated again. This results in a ratio of the squares of these radii of 2.14. In addition, the sample is tilted by  $45^\circ$  from the incoming beam during the pressure measurement, so we add a factor of  $\cos(45^\circ)$  resulting in a total geometry factor of 1.51. This leads to an initial charge carrier density of  $6.05 \cdot 10^{14} \text{ cm}^{-3}$

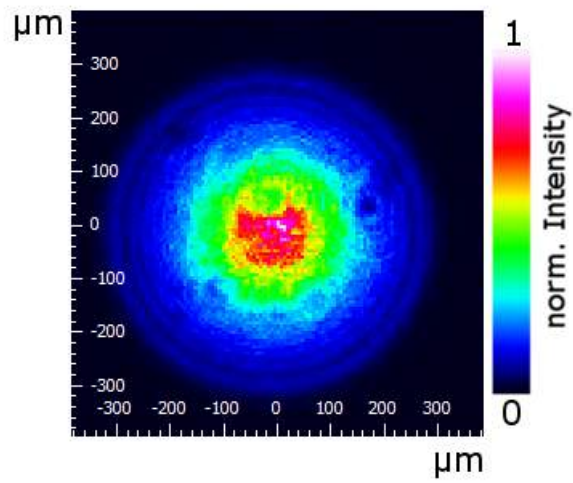


Figure 23: Distribution of power in the beam, measured with a Thorlabs beam profiler. Measured in air with the same distance of lens to sample as in the TCSPC-measurement



The indirect bandgap of [MAPI](#) also affects the absorption of light. Further proof for the existence of the indirect bandgap can be gathered by analyzing absorbance spectra. Since the efficient direct transition of absorption of light is still accessible, the less effective indirect transition will be a minor effect. Consequently, absorption data from an Ultraviolet-Visible light absorbance ([UV-Vis](#)) -as the one used by TianYi Wang in an earlier experiment- for pressure dependent absorption measurements are not suitable for detecting a possible indirect transition.

*Can we see the indirect transition in the absorption?*

However, [PDS](#) data is reported by Sadhanala et al. on [MAPI](#) [30]. [PDS](#) is a sensitive absorption measurement technique that uses the deflection of a laser beam in liquid due to the heating of the material upon light absorption. The heating of the material is solely induced by the absorption of a second laser beam, excluding reflection and scattering effects. The data from [30] is extracted via the website <http://arohatgi.info/WebPlotDigitizer/>.

In the following the data will be analyzed using the Tauc-formalism.

#### 4.1 INTRODUCTION TO TAUC RULE

First derived for amorphous silicon, the Tauc rule describes the absorption edge for direct and indirect semiconductors dependent on incident light energy. The formula is:

$$\alpha E = A_r (E - E_G)^r \quad (18)$$

where

- $\alpha$  absorbance<sup>1</sup>
- $E$  Energy of incident light
- $A_r$  proportionality factor for different  $r$  values
- $E_G$  Bandgap energy
- $r = 2$  coefficient for *indirect* allowed transition
- $r = \frac{1}{2}$  coefficient for *direct* allowed transition

A good derivation of the coefficients and an overview of the theory can be found in [31]. The derivation assumes that the absorption process is governed by a matrix element constant in energy. Additionally, the bandedges are assumed to be parabolic in the first approximation.

<sup>1</sup>  $\alpha = -\log_{10}(T)$ ;  $T$  is the transmittance

#### 4.2 PHONON ENERGY

The energy contribution of the phonon is neglected in this treatment, since the momentum difference is small, leading to an especially small energy when using the acoustic phonon dispersion relation, as shown below.

The phonon momentum can be calculated by assuming two parabolic bands that have a 60 meV difference from the  $k = 0$  point and the band edge. The curvature of the parabolic bands is determined by the effective masses, taken from [32]. The resulting wave vector is  $k_{\text{parabolic}} = 0.048 \text{ \AA}^{-1}$ . This value is comparable to  $k_{\text{Azar.}} \approx 0.05 \text{ \AA}^{-1}$  from [12]. To calculate the energy of an acoustic phonon with this wavevector I use the dispersion relation from Kittel[33] in eq.(19)

$$\omega = 2\sqrt{\frac{\gamma}{M}} \left| \sin\left(\frac{ka}{2}\right) \right| \quad (19)$$

where

- $\omega$  angular frequency
- $\gamma$  force constant
- $M$  mass of unit cell
- $k$  phonon wavevector
- $a$  lattice parameter

The force constant  $\gamma$  is connected to Young's modulus  $Y$  and the lattice parameter  $a$  *via*  $\gamma = Ya$ . The Young's modulus was derived from the phonon dispersion relation in [34] and found to be  $Y = (13 \pm 2) \text{ GPa}$ . The lattice parameter is  $a = 6.4 \text{ \AA}$  [35]. The mass of the unit cell is the sum of all unit cell constituents. These values lead to a phonon energy of 0.6 meV, for a phonon with momentum such that the indirect transition can occur. This represents 1% of the Rashba energy split and is therefore negligible.

#### 4.3 LINEARIZATION OF DATA WITH FIT

To find the appropriate parameters in Eq. (18), the data was linearized by solving Formula (18) for  $A(E - E_G)$  with the corresponding values for the  $r$ -coefficient. The range of datapoints that exhibit linear behavior obey the Tauc-formula. The appropriate linear range is selected by hand to execute a linear fit. The result can be seen in Fig. 24. It has to be noted that the linearity of the data only shows that *part* of the data can be described by Taucs rule; it is still yet to be demonstrated that the whole absorption edge is correctly described. The approximation of parabolic bands is only valid in the direct vicinity around the band edge minimum.



The linear fits supply the values for  $A_r$  and  $E_G$  which allows the plotting of the curves in the original absorbance plot (Fig.25).

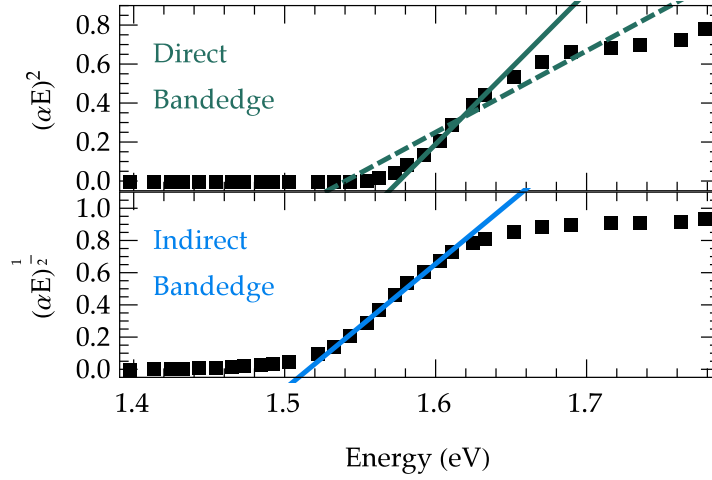


Figure 24: Linearization of absorbance data according to the Tauc rule for direct and indirect band edges with linear fits (eq.(18)). Dashed line in the upper graph is an attempt to describe the whole band edge with a direct band edge.

#### 4.4 URBACH TAIL

In all absorption data an exponential tail (Urbach Tail) can be found. This is a process mostly assigned to shallow traps, Gaussian disorder in the material from grain to grain variation, and thermal vibrations [36]. This tail is associated with an energy, the Urbach energy. The variation of the band structure means that this process will influence the low energy side of the band edge where the process is not competing with band to band absorption. I fit the low energy tail of the absorption data with an exponential curve. The fit is good, as seen by a random distribution of the residuals. The extracted Urbach energy is 21 meV, comparable to 15 meV measured before [37].

#### 4.5 RESULTING ABSORBANCE PLOT

It is clear from Fig.25 that the low energy data can only be described by an indirect band edge. The position of the exponential tail is clear and distinct from the indirect or direct band edge. An attempt to fit the band edge with only the direct absorption transition as shown in the dashed line yields a poor fit. The difference between the direct and indirect bandgap energy is 60 meV, agreeing with theory and the PL measurement, which is additional strong evidence in favor of the existence of an indirect transition.

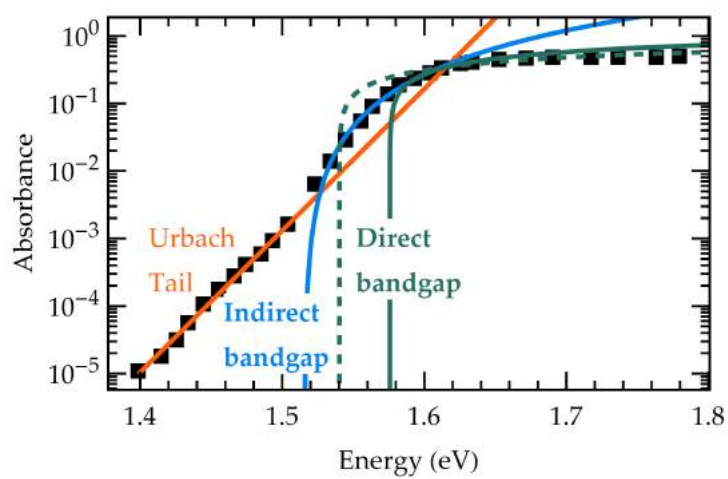


Figure 25: PDS data from literature [30] fitted with an exponential Urbach tail (orange), an indirect (blue), and direct (green) bandgap. A fit of a direct bandgap only is shown in dashed green

## ELECTRICAL PROPERTIES OF MAPI UNDER PRESSURE

Pressure induces a change in crystal structure, and consequently a change in band structure. This change should also influence the transport of electrons. I present pressure dependent resistance measurements under illumination and in the dark, and bandgap theory that describes the dark measurement.

### 5.1 SETUP

We measure Current Voltage (IV) characteristics of MAPI under pressure. The sample measured consists of a  $\sim 300\text{nm}$  thick MAPI layer on a glass slide. A gold layer of  $80\text{nm}$  is evaporated, with a  $120\mu\text{m}$  wide gap<sup>1</sup> as defined by a  $120\mu\text{m}$  thick wire acting as a shadow mask (Fig. 26). The edges of the gold electrode are connected with aluminum legs. These legs in turn are fixed with epoxy glue and dried for at least 2 h to ensure hardening. The connection between the legs and the gold electrode is improved by applying conductive silver paint. The aluminum legs are then connected to a plug with an electrical feed through, that allows for electrical connection under high pressure (Fig. 26).

*How does the resistance change with pressure?*

The measurement was conducted as shown in Schematics 27.

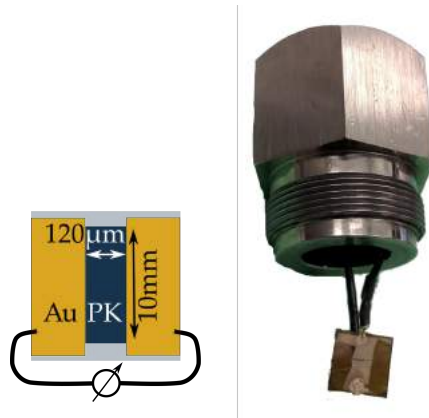


Figure 26: *Left* sketch and *right* photo of the material used for the resistance measurement.

The IV-Curves were measured with a Keithley 2401 SMU that scanned the voltage from  $-10\text{V}$  to  $10\text{V}$ . One IV-Scan took 1:30 min.

<sup>1</sup> measured with an optical microscope



Figure 27: Measurement protocol of the resistance measurement.

## 5.2 MEASUREMENT IN THE DARK

Fig 28 shows the raw data measured in the dark. The resistance follows Ohms law since there is a linear relationship between current and voltage. The noise of the measurement stems from our small current of nano-amperes and the use of unshielded banana cable. It is in fact crucial that the measurement is not disturbed by people walking by. The resistance drops at higher pressure. To quantify the resistance we fit a linear equation to the data, using LinearModelFit in Mathematica 10.3 and extracting the resistance from the slope. The resistance halves with higher pressure, from 40 G $\Omega$  to 20 G $\Omega$  at 400 MPa, with no clear phase transition at 320 MPa.

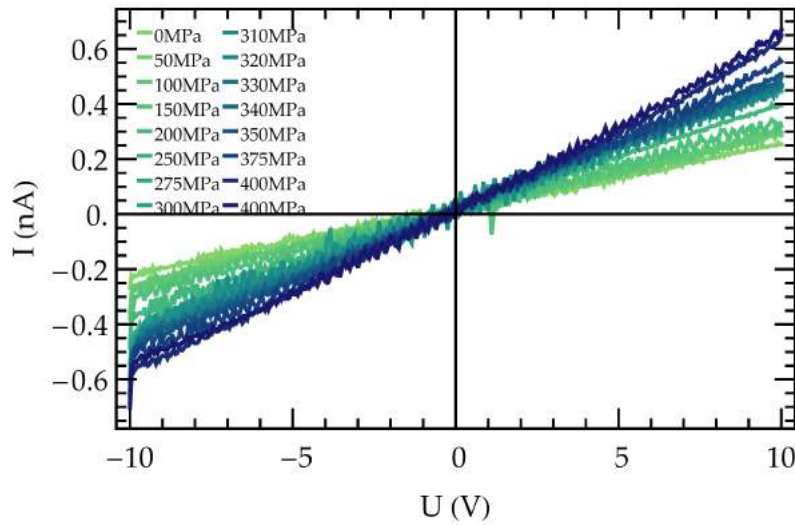


Figure 28:  $I$ - $U$ -Curves taken at different pressures, without illumination. The device shows Ohmic behavior.

### 5.2.1 Theory

The trend of the resistance seen in the experimental data could be explained by a change of the intrinsic charge carrier density, caused by a change of bandgap energy. The temperature of the sample is assumed to stay constant, meaning the Fermi energy level<sup>2</sup> of the

<sup>2</sup> energy level up to which electrons occupy all states

material stays constant as well. The intrinsic charge carrier density is described by standard semiconductor theory [33] as seen in Rq. (20).

$$n_i = 2 \left( \frac{k_B T}{2\pi\hbar^2} \right)^{\frac{3}{2}} (m_e^* m_h^*)^{\frac{3}{4}} \exp \left( -\frac{E_G}{2k_B T} \right) \quad (20)$$

where

- $n_i$  intrinsic charge carrier density
- $k_B$  Boltzmann constant
- $T$  temperature
- $m_e^*$  effective mass of electron
- $m_h^*$  effective mass of hole
- $E_G$  electronic bandgap

We assume that the effective mass of electrons and holes do not change and that there is no doping.

The conductivity is given by:

$$\sigma = n_i (\mu_e + \mu_h) q \quad (21)$$

where

- $\sigma$  conductivity
- $n_i$  intrinsic charge carrier density
- $\mu_e$  mobility of electron
- $\mu_h$  mobility of hole
- $q$  elementary charge

Which leads to a resistance of

$$R = \frac{l}{\sigma A} = \frac{C_0}{\exp \left( -\frac{E_G}{2k_B T} \right)} \quad (22)$$

where

- $R$  resistance
- $l$  length of the gap
- $\sigma$  conductivity
- $A$  cross sectional area  
(height of the sample  $\times$  length of the gap)
- $C_0$  scaling constant

Absorption measurements of [MAPI](#) under pressure, executed by TianYi Wang, supply us with the value of the band gap energy as a function of pressure.  $C_0$  is obtained by setting Eq. (22) to the resistance value

at 0 MPa and solving for  $C_0$  by using the known bandgap and temperature. The other data points in Fig.29 are calculated by using Eq. 22 with different band gap energies.

### 5.2.2 Fit of Theory

Theory describes the data points before the phase transition well, suggesting the change in bandgap as the main cause for the smaller resistance under pressure. Since there are significant structural changes in the crystal during the phase transition to the high pressure phase<sup>3</sup>, the description of the points above phase transition fails.

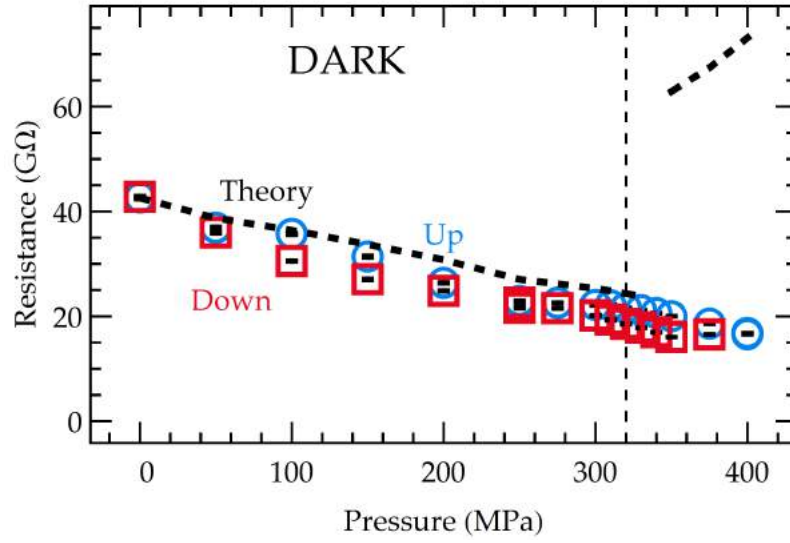


Figure 29: Resistance without illumination, as function of hydrostatic pressure. Theory curve following Eq. (22). Black bars represent error bars derived from the fit error.

### 5.2.3 Direct calculation using literature parameters

All parameters of Eq. (21) are also known to us from literature. This allows for the direct computation of the intrinsic charge carrier density and consequently, the resistance. The mobilities are taken from [28], and effective masses are taken from [11]. At ambient temperature there are  $n_i = 7.5 \times 10^4 \text{ cm}^{-3}$  intrinsic charge carriers, according to Eq. (20). Using formulas (21) and (22) we can calculate the expected resistance, having a value of  $R_{n_i} = 2.5 \times 10^{15} \Omega$ . This value is six orders of magnitude higher than measured in the experiment. This discrepancy might be explained by introducing an additional charge

<sup>3</sup> which have strong influences on the electrical properties besides the change in bandgap

carrier density induced by doping. To explain the measured resistance the doping charge carrier density would need to be  $n_{\text{doping}} = 4 \times 10^9 \text{ cm}^{-3}$ . Eq. (21) captures only the intrinsic charge carrier density. An additional complication might be a change in Fermi energy level. In the resistance calculation (eq. (22)) the Fermi energy level and the valence band are assumed to be constant with changing pressure, only the conduction band is changing its energy level.

Resistance values derived from Eq. (22) can therefore only be an approximation.

### 5.3 MEASUREMENT UNDER ILLUMINATION

The sample is illuminated by a white Thorlabs LED with the power of approximately 0.12 Sun<sup>4</sup>, leading to a high density of photo induced charge carriers, seen by the one order of magnitude smaller resistance in the  $\sim \text{M}\Omega$  regime.

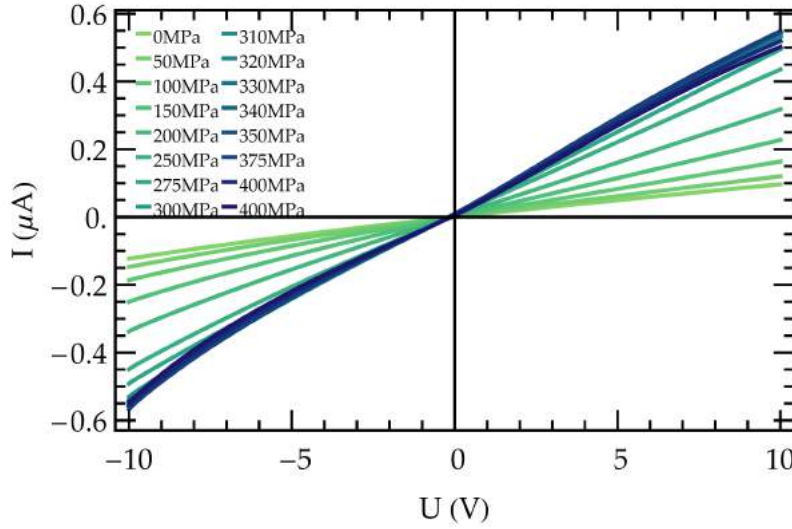


Figure 30:  $IV$ -Curves taken at different pressures, under 0.1 sun LED illumination. The device shows Ohmic behavior.

**EXPERIMENTAL RESULTS** The device also shows ohmic behavior under illumination, but there is a slight deviation from a perfect linear relationship (Fig. 30). As in the previous measurement, the resistance value is extracted from a linear fit. The resistance drops with higher pressure, as in the dark measurement. The decrease in resistance is larger in the measurement under illumination, starting at  $85 \text{ M}\Omega$  and ending at  $20 \text{ M}\Omega$ .

<sup>4</sup> determined from a comparison of the silicon photo-diode photo-current induced by the LED and a solar simulator

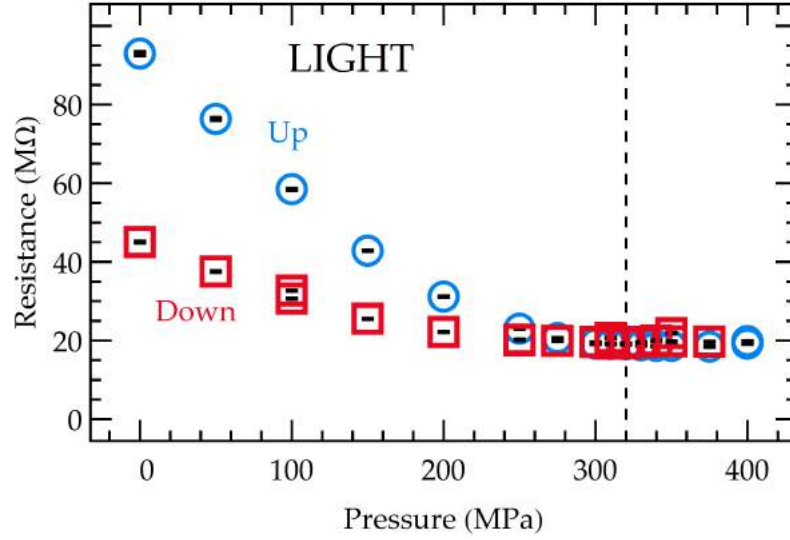


Figure 31: Resistance extracted via a linear fit to the *IV*-Curves, taken at different pressures under illumination. Black bars represent error bars derived from the fit error.

Since the bandgap of *MAPI* is at  $\sim 800\text{nm}$  and the red, blue, and green *LEDs* making up the white light are of far lower wavelength, the change in bandgap has no influence on the number of absorbed photons. Therefore, it should be possible to describe the trend we see by adding a constant term of photoinduced charge carriers to the intrinsic charge carriers. This approach was attempted and failed. The resistance decreases much faster than predicted by Formula (22).

*Why is does the resistance under light decrease so much?*

One possible cause for this strong decrease in resistance could be heating induced by illumination of 0.1 sun intensity. However the photo-induced charge carriers are not following a temperature-dependent Fermi Dirac distribution.

If there is in fact considerable doping, as described above, there might be a significant heat-induced change in free charge carriers. The amount of charge carriers above the Fermi level changes linearly with temperature, as seen by calculating the integral  $\int_{E_{\text{Fermi}}}^{\infty} F(E, T) dE \propto T$ . By assuming a heating of 40 K we can see that the charge carrier density would increase by only 13%. Since the resistance is proportional to the charge carrier density, this explanation is unlikely to explain the data fully.

The bands change their curvature under pressure, meaning that the effective masses of the electrons and holes cannot be treated as constant. Most likely this is a minor effect, because if it would play a considerable role, this effect would also be visible in the dark measurement. Without illumination there seems to be no deviation from the theory with constant effective mass, rendering this explanation



unlikely.

**HYSTERESIS** There is a large hysteresis in the illuminated resistance measurement between the pressure up- and down-stroke as seen in Fig. 31. The resistance reduces by a factor of two after the measurement. This is surprising since the pressure-induced change in band structure and the optoelectronic properties are reversible. Also, the resistance measurements in the dark and under illumination differ, with the dark resistance curve being hysteresis free. The effect responsible for the hysteresis can therefore only affect the properties under illumination. Also, repeating the measurement at one pressure point gives the same result (seen from the measurement point at 100 MPa in the down stroke). In fact, the timescale for the material to relax back to the initial high resistance state is days, as shown by repeating the measurement three days later.

*Why is there a strong hysteresis?*

These above described properties were reproduced in a repeat measurement.

The scanning direction has no influence on the hysteresis, ruling out a preferred alignment of the MA-dipoles on a long timescale. Here, it also has to be noted that the fields in our sample are much smaller than in a working solar cell. A solar cell with typical thickness of  $1\text{ }\mu\text{m}$  and a voltage of  $\sim 1\text{ V}$  has an internal field of  $1 \times 10^6\text{ Vm}^{-1}$ , whereas our device has a distance of  $\sim 120\text{ }\mu\text{m}$  and a voltage of  $10\text{ V}$  resulting in a field of  $\sim 8 \times 10^4\text{ Vm}^{-1}$ , two orders of magnitude lower than in the solar cell. This difference means that the MA dipoles will also align much less in our sample than in a working solar cell [38], rendering the influence of the dipole an unlikely explanation of the big and long timescale hysteresis.

One reason for the hysteresis in IV-Curves of MAPI solar cells is ion migration [39], a conceivable explanation for our hysteresis. However, ion migration would happen on a much shorter timescale of minutes, which would appear in the IV-scan but not on days as is exhibited in this work.

The IV-curves themselves do not exhibit hysteresis, as tested in a separate experiment. A voltage sweep from  $-10\text{ V}$  to  $10\text{ V}$  to  $-10\text{ V}$  shows no IV-hysteresis loop, suggesting that the mechanism for the pressure hysteresis is not the same as the one commonly found for IV hysteresis in MAPI solar cells.

Changes of grain structure could lead to changes in charge carrier transport. The inter-grain optoelectronic properties we probe via TCSPC and PL measurements would not be affected by this, explaining the lack of hysteresis in these measurements. The fact that only the resistance measurement under illumination shows hysteresis might point towards charge carrier saturation effects.

The underlying mechanism for the long timescale effect lowering the resistance of photoinduced charge carriers after being exposed to high pressure stays elusive.

## CONCLUSION AND OUTLOOK

---

### 6.1 CONCLUSION

This work supplies the first experimental evidence of an indirect bandgap in [MAPI](#). In [PL](#)-spectra a side peak has been observed that is ascribed to an indirect bandgap 60 meV below the direct transition. The strength of the [PL](#) side peak signal becomes stronger under hydrostatic pressure due to a change in the band structure. The difference in energy between the main peak and the side peak decreases from 60 meV to 50 meV, which is consistent with the trend expected within our model. The existence of an indirect bandgap is further backed by a doubling in photoluminescence quantum yield under pressure, which can be explained by the more direct nature of the bandgap, requiring a smaller energy phonon assistance for the transition to occur. [PDS](#) absorbance data of the same material taken by another group has been reanalyzed and an indirect bandgap was found to explain the absorbance data.

The resistance of [MAPI](#) under pressure has been measured both in the dark and under illumination and an attempt has been made to explain the data without illumination by a change in charge carrier density.

The existence of an indirect bandgap can explain the seemingly contradictory properties of [MAPI](#) of both strong absorption (*via* an direct transition) and long carrier lifetime (*via* photo induced carrier relaxation to an indirect band edge). Therefore, it offers a substantial new insight to the key mechanism that allows for high efficiency [MAPI](#) solar cells.

### 6.2 OUTLOOK

The measurement of working solar cell devices under pressure has been attempted but failed ultimately due to additional soft layers necessary in the device design. This led to a break in contact. Future work could include the use of hard inorganic hole extracting layers that are less susceptible to degradation through pressure.

Another interesting path is the investigation of the generality of the indirect bandgap model by exchanging the lead atom with other, less

dense materials. This should reduce the spin orbit coupling and lead to a smaller Rashba splitting.

The organic MA ion can be replaced for a molecule with a lesser dipole moment (FA has 0.2 Debye, MA has 2.3 Debye [32], Cesium has no dipole moment) which should decrease the lift in degeneracy of the Rashba spin split if the MA dipole plays a significant role for the electric field. A higher dipole moment, resulting in a stronger Rashba splitting could be achieved by fluorination of the MA ion into  $\text{CF}_3\text{NH}_3^+$ , which is predicted to have a dipole moment of 6.6 Debye [32]. However, this route might be practically unfeasible, since the fluorination process of MA, needed to produce this compound, is challenging and the product is unstable [40]. These studies should allow for a broader insight into importance of Rashba splitting in perovskite structures in general.

Recently, a direct measurement of Rashba split in  $\text{MAPbBr}_3$  via angle-resolved photoelectron spectroscopy has been reported [41]. This measurement promises that the explanation of long charge carrier lifetime via an indirect band gap is also valid for other metal halide perovskites.

## BIBLIOGRAPHY

---

- [1] U.S. EIA. *The International Energy Outlook 2016*. 2016th ed. Vol. 0484. May. Washington, DC: U.S. Energy Information Administration, 2016. ISBN: 2025866135. URL: <http://www.eia.gov/forecasts/ieo/world.cfm> (cit. on p. 1).
- [2] L. M. Miller, F. Gans, and A. Kleidon. "Estimating maximum global land surface wind power extractability and associated climatic consequences." In: *Earth System Dynamics* 2.1 (2011), pp. 1–12. ISSN: 21904979. DOI: [10.5194/esd-2-1-2011](https://doi.org/10.5194/esd-2-1-2011) (cit. on p. 1).
- [3] Jeong-Hyeok Im, In-Hyuk Jang, Norman Pellet, Michael Grätzel, and Nam-Gyu Park. "Growth of  $\text{CH}_3\text{NH}_3\text{PbI}_3$  cuboids with controlled size for high-efficiency perovskite solar cells." In: *Nature nanotechnology* 9.11 (2014), pp. 927–932. ISSN: 1748-3395. DOI: [10.1038/nnano.2014.181](https://doi.org/10.1038/nnano.2014.181). URL: <http://www.ncbi.nlm.nih.gov/pubmed/25173829> (cit. on p. 1).
- [4] Xie Ziang et al. "Refractive index and extinction coefficient of  $\text{CH}_3\text{NH}_3\text{PbI}_3$  studied by spectroscopic ellipsometry." In: *Optical Materials Express* 5.1 (2014), p. 29. ISSN: 2159-3930. DOI: [10.1364/OME.5.000029](https://doi.org/10.1364/OME.5.000029). URL: <http://www.scopus.com/inward/record.url?eid=2-s2.0-84920984344%7B%5C%7DpartnerID=tZ0tx3y1> (cit. on p. 2).
- [5] Aurélien Leguy et al. "Experimental and theoretical optical properties of methylammonium lead halide perovskites." In: *Nanoscale* (2015), pp. 6317–6327. ISSN: 2040-3364. DOI: [10.1039/C5NR05435D](https://doi.org/10.1039/C5NR05435D). URL: <http://pubs.rsc.org/en/content/articlehtml/2015/nr/c5nr05435d> (cit. on p. 2).
- [6] Laura M Herz. "Charge carrier dynamics in organic-inorganic metal halide perovskites." In: *Annu. Rev. Phys. Chem.* 67. February (2016), pp. 1–25. DOI: [DOI: 10.1146/annurev-physchem-040215-112222](https://doi.org/10.1146/annurev-physchem-040215-112222) (cit. on pp. 2, 3, 28).
- [7] Thomas M. Brenner, David a. Egger, Leeor Kronik, Gary Hodes, and David Cahen. "Hybrid organic—inorganic perovskites: low-cost semiconductors with intriguing charge-transport properties." In: *Nature Reviews Materials* 1.1 (2016), p. 15007. ISSN: 2058-8437. DOI: [10.1038/natrevmats.2015.7](https://doi.org/10.1038/natrevmats.2015.7). URL: <http://www.nature.com/articles/natrevmats20157> (cit. on p. 3).
- [8] Hong Hua Fang, Raissa Raissa, Mustapha Abdu-Aguye, Sampson Adjokatse, Graeme R. Blake, Jacky Even, and Maria Antonietta Loi. "Photophysics of organic-inorganic hybrid lead

- iodide perovskite single crystals." In: *Advanced Functional Materials* 25.16 (2015), pp. 2378–2385. ISSN: 16163028. DOI: [10.1002/adfm.201404421](https://doi.org/10.1002/adfm.201404421) (cit. on p. 4).
- [9] X. Y. Zhu and V. Podzorov. "Charge Carriers in Hybrid Organic-Inorganic Lead Halide Perovskites Might Be Protected as Large Polarons." In: *Journal of Physical Chemistry Letters* 6.23 (2015), pp. 4758–4761. ISSN: 19487185. DOI: [10.1021/acs.jpclett.5b02462](https://doi.org/10.1021/acs.jpclett.5b02462) (cit. on p. 4).
- [10] Dane W de Quilettes, Sarah M Vorpahl, Samuel D Stranks, Hirokazu Nagaoka, Giles E Eperon, Mark E Ziffer, Henry J Snaith, David S Ginger, and David S. Ginger<sup>1†</sup> Dane W. deQuilettes Sarah M. Vorpahl Samuel D. Stranks Hirokazu Nagaoka Giles E. Eperon Mark E. Ziffer Henry J. Snaith. "Impact of microstructure on local carrier lifetime in perovskite solar cells." In: *Science* 348.6235 (May 2015), pp. 1689–1699. ISSN: 1098-6596. DOI: [10.1126/science.aaa5333](https://doi.org/10.1126/science.aaa5333). arXiv: [arXiv:1011.1669v3](https://arxiv.org/abs/1011.1669v3). URL: <http://science.sciencemag.org/content/348/6235/683.abstract> (cit. on p. 5).
- [11] Federico Brivio, Keith T. Butler, Aron Walsh, and Mark van Schilfgaarde. "Relativistic quasiparticle self-consistent electronic structure of hybrid halide perovskite photovoltaic absorbers." In: *Physical Review B* 89.15 (Apr. 2014), p. 155204. ISSN: 1098-0121. DOI: [10.1103/PhysRevB.89.155204](https://doi.org/10.1103/PhysRevB.89.155204). arXiv: [/arxiv.org/abs/1401.6993](https://arxiv.org/abs/1401.6993) [http:]. URL: <http://link.aps.org/doi/10.1103/PhysRevB.89.155204> (cit. on pp. 5, 11, 42).
- [12] Pooya Azarhoosh, Jarvist M. Frost, Scott McKechnie, Aron Walsh, and Mark van Schilfgaarde. "Relativistic origin of slow electron-hole recombination in hybrid halide perovskite solar cells." In: *arXiv* (2016), pp. 1–17. arXiv: [1604.04500](https://arxiv.org/abs/1604.04500). URL: <http://arxiv.org/abs/1604.04500> (cit. on pp. 5, 7, 14, 36).
- [13] Mikaël Kepenekian, Roberto Robles, Claudine Katan, Daniel Saponi, Laurent Pedesseau, Jacky Even, Sciences Chimiques, Campus Uab, and Foton Umr. "Rashba and Dresselhaus Effects in Hybrid Organic À Inorganic Perovskites: From Basics to Devices." In: *ACS Nano* 9.12 (2015), pp. 11557–11567. ISSN: 1936-0851. DOI: [10.1021/acs.nano.5b04409](https://doi.org/10.1021/acs.nano.5b04409) (cit. on p. 5).
- [14] Xiuwen Zhang, Qihang Liu, Jun-Wei Luo, Arthur J. Freeman, and Alex Zunger. "Hidden spin polarization in inversion-symmetric bulk crystals." In: *Nature Physics* 10.5 (2014), pp. 387–393. ISSN: 1745-2473. DOI: [10.1038/nphys2933](https://doi.org/10.1038/nphys2933). arXiv: [1402.4446](https://arxiv.org/abs/1402.4446). URL: <http://dx.doi.org/10.1038/nphys2933> (cit. on p. 6).
- [15] Federico Brivio, Jarvist M. Frost, Jonathan M. Skelton, Adam J. Jackson, Oliver J. Weber, Mark T. Weller, Alejandro R. Goñi, Aurélien M A Leguy, Piers R F Barnes, and Aron Walsh. "Lattice dynamics and vibrational spectra of the orthorhombic, tetrag-

- onal, and cubic phases of methylammonium lead iodide.” In: *Physical Review B - Condensed Matter and Materials Physics* 92.14 (2015), pp. 1–9. ISSN: 1550235X. DOI: [10.1103/PhysRevB.92.144308](https://doi.org/10.1103/PhysRevB.92.144308). arXiv: [arXiv:1504.07508v2](https://arxiv.org/abs/1504.07508v2) (cit. on pp. 6, 7, 15).
- [16] F. J. Manjon, A. Segura, V. Munoz-Sanjose, G. Tobias, P. Ordejon, and E. Canadell. “Band structure of indium selenide investigated by intrinsic photoluminescence under high pressure.” In: *Physical Review B - Condensed Matter and Materials Physics* 70.12 (2004), pp. 1–12. ISSN: 01631829. DOI: [10.1103/PhysRevB.70.125201](https://doi.org/10.1103/PhysRevB.70.125201) (cit. on p. 8).
- [17] D. Errandonea, E. Bandiello, A. Segura, J. J. Hamlin, M. B. Maple, P. Rodriguez-Hernandez, and A. Muñoz. “Tuning the band gap of PbCrO<sub>4</sub> through high-pressure: Evidence of wide-to-narrow semiconductor transitions.” In: *Journal of Alloys and Compounds* 587 (2014), pp. 14–20. ISSN: 09258388. DOI: [10.1016/j.jallcom.2013.10.179](https://doi.org/10.1016/j.jallcom.2013.10.179). URL: <http://dx.doi.org/10.1016/j.jallcom.2013.10.179> (cit. on p. 8).
- [18] Zeyu Deng, Fengxia Wei, Shijing Sun, Gregor Kieslich, Anthony K. Cheetham, and Paul D. Bristowe. “Exploring the properties of lead-free hybrid double perovskites using a combined computational-experimental approach.” In: Figure 1 (2016), arXiv:1606.02916. arXiv: [1606.02916](https://arxiv.org/abs/1606.02916). URL: <http://arxiv.org/abs/1606.02916> (cit. on p. 8).
- [19] Adam Jaffe, Yu Lin, Christine M. Beavers, Johannes Voss, Wendy L. Mao, and Hemamala I. Karunadasa. “High-Pressure Single-Crystal Structures of 3D Lead-Halide Hybrid Perovskites and Pressure Effects on their Electronic and Optical Properties.” In: *ACS Central Science* (2016), acscentsci.6b00055. ISSN: 2374-7943. DOI: [10.1021/acscentsci.6b00055](https://doi.org/10.1021/acscentsci.6b00055). URL: <http://dx.doi.org/10.1021/acscentsci.6b00055> (cit. on pp. 11, 12).
- [20] Shaojie Jiang et al. “Pressure-Dependent Polymorphism and Band-Gap Tuning of Methylammonium Lead Iodide Perovskite.” In: *Angewandte Chemie - International Edition* (2016), pp. 6540–6544. ISSN: 15213773. DOI: [10.1002/anie.201601788](https://doi.org/10.1002/anie.201601788) (cit. on p. 11).
- [21] Joseph S Manser and Prashant V Kamat. “Band filling with free charge carriers in organometal halide perovskites.” In: *Nat. Photonics* 8.August (2014), Ahead of Print. ISSN: 1749-4885. DOI: [10.1038/nphoton.2014.171](https://doi.org/10.1038/nphoton.2014.171). URL: <http://www.nature.com/nphoton/journal/vaop/ncurrent/pdf/nphoton.2014.171.pdf> (cit. on p. 14).
- [22] Gert Jan A H Wetzelaer, Max Scheepers, Araceli Miquel Sempere, Cristina Momblona, Jorge ??vila, and Henk J. Bolink. “Trap-Assisted Non-Radiative Recombination in Organic-Inorganic Perovskite Solar Cells.” In: *Advanced Materials* 27.11 (2015), pp. 1837–

1841. ISSN: 15214095. DOI: [10.1002/adma.201405372](https://doi.org/10.1002/adma.201405372) (cit. on pp. [15](#), [20](#), [21](#)).
- [23] D. Bi et al. "Efficient luminescent solar cells based on tailored mixed-cation perovskites." In: *Science Advances* 2.1 (2016), e1501170–e1501170. ISSN: 2375-2548. DOI: [10.1126/sciadv.1501170](https://doi.org/10.1126/sciadv.1501170). URL: <http://advances.sciencemag.org/content/2/1/e1501170.abstract> <http://advances.sciencemag.org/cgi/doi/10.1126/sciadv.1501170> (cit. on p. [21](#)).
- [24] Rene Andrae, Tim Schulze-Hartung, and Peter Melchior. "Dos and don'ts of reduced chi-squared." In: *Astro-Ph* (2010), p. 12. arXiv: [1012.3754](https://arxiv.org/abs/1012.3754). URL: <http://arxiv.org/abs/1012.3754> (cit. on p. [23](#)).
- [25] Ronald L. Wasserstein and Nicole A. Lazar. "The ASA's statement on p-values: context, process, and purpose." In: *The American Statistician* 1305.April (2016), pp. 00–00. ISSN: 0003-1305. DOI: [10.1080/00031305.2016.1154108](https://doi.org/10.1080/00031305.2016.1154108). arXiv: [1011.1669](https://arxiv.org/abs/1011.1669). URL: <http://www.tandfonline.com/doi/full/10.1080/00031305.2016.1154108> (cit. on p. [23](#)).
- [26] Christian Wehrenfennig, Giles E. Eperon, Michael B. Johnston, Henry J. Snaith, and Laura M. Herz. "High charge carrier mobilities and lifetimes in organolead trihalide perovskites." In: *Advanced Materials* 26.10 (2014), pp. 1584–1589. ISSN: 15214095. DOI: [10.1002/adma.201305172](https://doi.org/10.1002/adma.201305172) (cit. on p. [24](#)).
- [27] A. Köhler and H. Bässler. "Triplet states in organic semiconductors." In: *Materials Science and Engineering: R: Reports* 66.4-6 (2009), pp. 71–109. ISSN: 0927796X. DOI: [10.1016/j.mser.2009.09.001](https://doi.org/10.1016/j.mser.2009.09.001). URL: <http://linkinghub.elsevier.com/retrieve/pii/S0927796X09000886> (cit. on p. [26](#)).
- [28] Carlo Motta, Fedwa El-Mellouhi, and Stefano Sanvito. "Charge carrier mobility in hybrid halide perovskites." In: *Scientific reports* 5 (2015), p. 12746. ISSN: 2045-2322. DOI: [10.1038/srep12746](https://doi.org/10.1038/srep12746). arXiv: [arXiv: 1411.7904v2](https://arxiv.org/abs/1411.7904v2). URL: <http://www.pubmedcentral.nih.gov/articlerender.fcgi?artid=4522682%7B%5C%7Dtool=pmcentrez%7B%5C%7Drendertype=abstract> (cit. on pp. [28](#), [42](#)).
- [29] Felix Deschler et al. "High photoluminescence efficiency and optically pumped lasing in solution-processed mixed halide perovskite semiconductors." In: *Journal of Physical Chemistry Letters* 5.8 (2014), pp. 1421–1426. ISSN: 19487185. DOI: [10.1021/jz5005285](https://doi.org/10.1021/jz5005285) (cit. on p. [31](#)).
- [30] Aditya Sadhanala et al. "Preparation of Single Phase Films of  $\text{CH}_3\text{NH}_3\text{Pb}(\text{I}_{1-x}\text{Br}_x)_3$  with Sharp Optical Band Edges." In: *The Journal of Physical Chemistry Letters* (2014), p. 140709102712008.



- ISSN: 1948-7185. DOI: [10.1021/jz501332v](https://doi.org/10.1021/jz501332v). URL: <http://dx.doi.org/10.1021/jz501332v> (cit. on pp. 35, 38).
- [31] Peter Y Yu and Manuel Cardona. *Fundamentals of Semiconductors*. Vol. 1. 11. 2010, p. 793. ISBN: 978-3-642-00709-5. DOI: [10.1007/978-3-642-00710-1](https://doi.org/10.1007/978-3-642-00710-1). arXiv: [arXiv:1011.1669v3](https://arxiv.org/abs/1011.1669v3). URL: <http://www.springerlink.com/index/10.1007/978-3-642-00710-1> (cit. on p. 35).
- [32] Jarvist M. Frost, Keith T. Butler, Federico Brivio, Christopher H. Hendon, Mark Van Schilfgaarde, and Aron Walsh. "Atomistic origins of high-performance in hybrid halide perovskite solar cells." In: *Nano Letters* 14.5 (2014), pp. 2584–2590. ISSN: 15306992. DOI: [10.1021/nl500390f](https://doi.org/10.1021/nl500390f). arXiv: [1402.4980](https://arxiv.org/abs/1402.4980) (cit. on pp. 36, 48).
- [33] C Kittel. *Introduction to Solid State Physics*. Vol. 8th editio. 2004, p. 704. ISBN: 047141526X. DOI: [citeulike-article-id:4202357](https://doi.org/citeulike-article-id:4202357). URL: <https://archive.org/details/IntroductionToSolidStatePhysics> (cit. on pp. 36, 41).
- [34] Alexander N Beecher, Octavi E Semonin, Jonathan M Skelton, Jarvist M Frost, W Maxwell, Haowei Zhai, Ahmet Alatas, Jonathan S Owen, Aron Walsh, and Simon J L Billinge. "The cubic phase of methylammonium lead iodide perovskite is not locally cubic." In: (2016), pp. 1–10. arXiv: [arXiv:1606.09267v1](https://arxiv.org/abs/1606.09267v1) (cit. on p. 36).
- [35] Takeo Oku. "Crystal Structures and Related Perovskite Compounds Used for Solar Cells." In: *Solar Cells - New Approaches and Reviews* (2015), pp. 77–101. ISSN: 978-953-51-2184-8. DOI: [10.5772/58490](https://doi.org/10.5772/58490). URL: <http://dx.doi.org/10.5772/59284> (cit. on p. 36).
- [36] V Sa-Yakant and H R Glyde. *Urbach Tails and Disorder*. 1987 (cit. on p. 37).
- [37] Stefaan De Wolf, Jakub Holovsky, Soo Jin Moon, Philipp L??per, Bjoern Niesen, Martin Ledinsky, Franz Josef Haug, Jun Ho Yum, and Christophe Ballif. "Organometallic halide perovskites: Sharp optical absorption edge and its relation to photovoltaic performance." In: *Journal of Physical Chemistry Letters* 5.6 (2014), pp. 1035–1039. ISSN: 19487185. DOI: [10.1021/jz500279b](https://doi.org/10.1021/jz500279b) (cit. on p. 37).
- [38] Giulia Grancini, Ajay Ram Srimath Kandada, Jarvist M Frost, Alex J Barker, Michele De Bastiani, Marina Gandini, Sergio Maras, Guglielmo Lanzani, Aron Walsh, and Annamaria Petrozza. "Role of microstructure in the electron–hole interaction of hybrid lead halide perovskites." In: *Nat Photon* 9.10 (2015), pp. 695–701. ISSN: 1749-4885. DOI: [10.1038/nphoton.2015.151](https://doi.org/10.1038/nphoton.2015.151) \rhttp://www.nature.com/nphoton/journal/v9/n10/abs/nphoton.

- 2015.151.html#supplementary-information. URL: <http://dx.doi.org/10.1038/nphoton.2015.151> (cit. on p. 45).
- [39] Yongbo Yuan, Jungseok Chae, Yuchuan Shao, Qi Wang, Zhengguo Xiao, Andrea Centrone, and Jinsong Huang. "Photovoltaic Switching Mechanism in Lateral Structure Hybrid Perovskite Solar Cells." In: *Advanced Energy Materials* 5.15 (2015), pp. 1–7. ISSN: 16146840. DOI: [10.1002/aenm.201500615](https://doi.org/10.1002/aenm.201500615) (cit. on p. 45).
- [40] Amanda F. Baxter, Karl O. Christe, and Ralf Haiges. "Convenient Access to  $\alpha$ -Fluorinated Alkylammonium Salts." In: *Angewandte Chemie - International Edition* 54.48 (2015), pp. 14535–14538. ISSN: 15213773. DOI: [10.1002/anie.201507177](https://doi.org/10.1002/anie.201507177) (cit. on p. 48).
- [41] Daniel Niesner, Max Wilhelm, Ievgen Levchuk, Andres Osvet, Shreetu Shrestha, Mirosław Batentschuk, Christoph Brabec, and Thomas Fauster. "Giant Rashba Splitting in  $\text{CH}_3\text{NH}_3\text{PbBr}_3$  Organic-Inorganic Perovskite." In: June (2016). arXiv: [1606.05867](https://arxiv.org/abs/1606.05867). URL: <http://arxiv.org/abs/1606.05867> (cit. on p. 48).

## COLOPHON

This document was typeset using the typographical look-and-feel `classicthesis` developed by André Miede. The style was inspired by Robert Bringhurst's seminal book on typography "*The Elements of Typographic Style*". `classicthesis` is available for both  $\text{\LaTeX}$  and  $\text{\LyX}$ :

<https://bitbucket.org/amiede/classicthesis/>

*Final Version* as of July 6, 2016 (`classicthesis` version 0.95).